



HAL
open science

A soft-chemistry approach to the synthesis of amorphous calcium ortho/pyrophosphate biomaterials of tunable composition

Laëtitia Mayen, Nicholai D Jensen, Danielle Laurencin, Olivier Marsan, Christian Bonhomme, Christel Gervais, Mark E. Smith, Cristina Coelho, Guillaume Laurent, Julien Trébosc, et al.

► To cite this version:

Laëtitia Mayen, Nicholai D Jensen, Danielle Laurencin, Olivier Marsan, Christian Bonhomme, et al.. A soft-chemistry approach to the synthesis of amorphous calcium ortho/pyrophosphate biomaterials of tunable composition. *Acta Biomaterialia*, 2020, 103, pp.333-345. 10.1016/j.actbio.2019.12.027. hal-02447805

HAL Id: hal-02447805

<https://hal.sorbonne-universite.fr/hal-02447805>

Submitted on 21 Jan 2020

HAL is a multi-disciplinary open access archive for the deposit and dissemination of scientific research documents, whether they are published or not. The documents may come from teaching and research institutions in France or abroad, or from public or private research centers.

L'archive ouverte pluridisciplinaire **HAL**, est destinée au dépôt et à la diffusion de documents scientifiques de niveau recherche, publiés ou non, émanant des établissements d'enseignement et de recherche français ou étrangers, des laboratoires publics ou privés.

A soft-chemistry approach to the synthesis of amorphous calcium ortho/pyrophosphate biomaterials of tunable composition

Laëtitia Mayen^{a,‡}, Nicolai D. Jensen^{b,c,‡}, Danielle Laurencin^b, Olivier Marsan^a, Christian Bonhomme^c, Christel Gervais^c, Mark E. Smith^d, Cristina Coelho^c, Guillaume Laurent^c, Julien Trebosc^e, Zhehong Gan^f, Kuizhi Chen^f, Christian Rey^a, Christèle Combes^a, Jérémy Soulié^{a*}

^aCIRIMAT, Université de Toulouse, CNRS, INPT-ENSIACET, Toulouse, France

^bICGM, CNRS-UM-ENSCM, Université de Montpellier, Montpellier, France

^cSorbonne Université, CNRS, LCMCP, Paris, France

^dDepartment of Chemistry, Lancaster University, Lancaster, UK

^eUniversité de Lille, UMR 8181, UCCS: Unit of Catalysis and Chemistry of Solids, Lille, France

^fNational High Magnetic Field Laboratory, Tallahassee, FL, USA

[‡]These authors contributed equally to the work.

*Corresponding author.

E-mail address: jeremy.soulie@toulouse-inp.fr

Abstract

The development of amorphous phosphate-based materials is of major interest in the field of biomaterials science, and especially for bone substitution applications. In this context, we herein report the synthesis of gel-derived hydrated amorphous calcium/sodium ortho/pyrophosphate materials at ambient temperature and in water. For the first time, such materials have been obtained in a large range of tunable orthophosphate/pyrophosphate molar ratios. Multi-scale characterization was carried out thanks to various techniques, including advanced multinuclear solid state NMR. It allowed the quantification of each ionic/molecular species leading to a general formula for these materials: $[(Ca^{2+}_y Na^+_z H^{3+x-2y-z})(PO_4^{3-})_{1-x}(P_2O_7^{4-})_x](H_2O)_u$. Beyond this formula, the analyses suggest that these amorphous solids are formed by the aggregation of colloids and that surface water and sodium could play a role in the cohesion of the whole material. Although the full comprehension of mechanisms of formation and structure is still to be investigated in detail, the straightforward synthesis of these new amorphous materials opens up many perspectives in the field of materials for bone substitution and regeneration.

Statement of Significance

The metastability of amorphous phosphate-based materials with various chain length often improves their (bio)chemical reactivity. However, the control of the ratio of the different phosphate entities has

not been yet described especially for small ions (pyrophosphate/orthophosphate) and using soft chemistry, whereas it opens the way for the tuning of enzyme- and/or pH-driven degradation and biological properties. Our study focuses on elaboration of amorphous gel-derived hydrated calcium/sodium ortho/pyrophosphate solids at 70°C with a large range of orthophosphate/pyrophosphate ratios. Multi-scale characterization was carried out using various techniques such as advanced multinuclear SSNMR (^{31}P , ^{23}Na , ^1H , ^{43}Ca). Analyses suggest that these solids are formed by colloids aggregation and that the location of mobile water and sodium could play a role in the material cohesion.

Keywords: Amorphous materials, mixed calcium ortho/pyrophosphate, soft chemistry, biomaterials

Introduction

Among inorganic materials for bone substitution, amorphous solids have attracted a lot of attention. Indeed, their metastability often improves their (bio)chemical reactivity. The subsequent release of active ions [1], and/or dissolution/precipitation reactions lead to neoformed apatite, that positively impacts osteoconduction and osteoinduction [2]. The most famous example of amorphous biomaterials is probably that of the bioactive silicate-based glasses (either sol-gel or melt-derived), which have been extensively studied [2,3]. The present paper, however, focuses on new types of phosphate-based amorphous materials for bone regeneration. Two main families of materials belonging to this category are studied by different scientific communities and are referenced in the literature as phosphate-based glasses and amorphous calcium phosphates.

On the one hand, phosphate-based glasses are generally made by fusion. Considering pure binary $\text{P}_2\text{O}_5\text{-CaO}$ glasses [4], the nature of the phosphate units (as expressed by the Q^n terminology,

where n is the number of bridging oxygen atoms per PO_4 tetrahedron) can be controlled through the atomic Ca/P ratio. This ratio can vary from ultraphosphates (phosphate 3D network mainly based on Q^3 species) to metaphosphate glasses (linear phosphate chains, mainly Q^2) and eventually to invert glasses (isolated pyrophosphates and orthophosphates, Q^1 and Q^0 respectively). This range of composition and the use of additives allow the elaboration of such glasses and the control of their dissolution [5-9].

On the other hand, amorphous calcium phosphate powders can be synthesized by precipitation in solution at room temperature, most of the time in water and without further high temperature treatment [10]. These are generally obtained by double decomposition between soluble calcium and phosphate salt precursors, and some processes lead to dense liquid “coacervates” [11]. Several kinds of phosphate precursors have been used: long-chain polyphosphates (polyP) [12,13], cyclic polyphosphates [14], diphosphates (also called pyrophosphates: $\text{P}_2\text{O}_7^{4-}$) [15-17] or orthophosphates (PO_4^{3-}) [10]. Without any high temperature treatment, the polyP associations are preserved in the final materials, which remain amorphous. In contrast, crystallization can occur when only orthophosphates or pyrophosphates (smaller anions) are present. In this case, the amorphous/crystalline nature depends on the synthetic parameters used (pH, concentration...) [16-18].

In this context, we recently reported the synthesis of different compositions of monolithic calcium and potassium pyrophosphate materials (PYG materials, PYrophosphate Glasses) prepared using soft conditions (in aqueous solution with a drying step at 70°C) [17]. We showed that an increase of the $\text{Ca}^{2+}/\text{P}_2\text{O}_7^{4-}$ ratio in the precursor batch solution resulted in an increase of the proportion of crystalline calcium pyrophosphate phase in the final material. This behavior was suggested to be induced by small amounts of orthophosphate ions formed by partial hydrolysis of the initial pyrophosphate entities during the synthesis process, which inhibited calcium pyrophosphate crystallization.

Considering this result, the aim of this paper is to present an original strategy for the low-temperature synthesis of gel-derived amorphous calcium phosphate materials (NaPYG) containing both pyrophosphate and orthophosphate entities in controlled amounts, and calcium and sodium as metal cations. To the best of our knowledge, this approach has never been described previously. Moreover, sodium phosphate salts were chosen here (in preference to the potassium ones), because sodium exhibits no side effects *in vivo* like hyperkalemia [19] (contrary to potassium).

Beyond the novelty of this synthesis, these mixed ortho/pyrophosphate materials appeared to us as potentially attractive candidates for bone substitution applications. Indeed, the interest of pure calcium pyrophosphate biomaterials has been demonstrated in the literature, through acellular and cellular *in vitro* tests [20,21], *in vivo* animal studies [22], and a clinical trial [23]. Pyrophosphates have been shown to hydrolyze *in vivo* by enzymatic reactions [20] and/or acidic pH [24] (due to inflammatory response after implantation), leading to orthophosphate ions, which are one of the key “building ions” of bone mineral. Pyrophosphate is one of the mineral ions considered to inhibit mineral formation. In osteoblast cultures especially, pyrophosphate inhibition occurs by binding to the mineral, up-regulating osteopontin, and inhibiting alkaline phosphatase activity [25.]. It has been observed, however, that, *in vivo*, the pyrophosphate level is rather well controlled and that its variations, due to physical activity for example, are regulated [26]. More generally, in humans, the total production of pyrophosphate ions per day is evaluated, from 0.7 to several kg [26] and more than 170 biological reactions involving pyrophosphate ions have been identified [26].

Therefore, the control of the ortho/pyrophosphate ratio within an amorphous material (synthesized at a temperature of only 70°C and without any additives) could potentially be an interesting adjustable parameter for tuning the kinetics of biomaterial degradation and bone mineral formation.

In this work, we thus investigate in detail the effect of the ortho/pyrophosphate content on the nature, structure and morphology of newly-synthesized amorphous biomaterials, using complementary characterization techniques and in particular advanced multinuclear solid state NMR. Advanced solid state NMR are of paramount importance in the studies of amorphous derivatives such as bioglasses for which XRD data are much less informative. The smart use of the NMR interactions (indirect J couplings and spatial dipolar couplings, D) allows to safely establish through-bond and through-space connectivities. In this work, ³¹P INADEQUATE MAS experiments were explored to disentangle the contributions of ortho- and pyrophosphates groups in 1D ³¹P MAS experiments (especially for amorphous materials). Most importantly, homo- (³¹P-³¹P) and heteronuclear (²³Na-³¹P) 2D correlation experiments were implemented to highlight the presence/absence of segregated domains (both from the anionic, ie ortho- and pyrophosphates, and cationic, ie Na⁺ and Ca²⁺, points of view).

Experimental section

Precursors

Calcium chloride dihydrate ($\text{CaCl}_2 \cdot 2\text{H}_2\text{O}$, Merck) and tri-sodium phosphate dodecahydrate ($\text{Na}_3\text{PO}_4 \cdot 12\text{H}_2\text{O}$, GRP rectapur, VWR Chemicals) were used as received, as calcium and orthophosphate sources, respectively. The pyrophosphate precursor, anhydrous tetrasodium pyrophosphate ($\text{Na}_4\text{P}_2\text{O}_7$), was prepared by heating disodium hydrogen phosphate powder (Na_2HPO_4 , VWR Chemicals) at 400°C during 15 hours in a muffle furnace. The formation of this salt was verified by XRD, Raman and ^{31}P solid state NMR spectroscopies before its use (in particular, no residual orthophosphate entity was detected by NMR).

Synthesis

Calcium and phosphate reagent solutions were prepared separately by dissolving $\text{CaCl}_2 \cdot 2\text{H}_2\text{O}$ in 40 mL of deionized water (solution A), and orthophosphate ($\text{Na}_3\text{PO}_4 \cdot 12\text{H}_2\text{O}$) and pyrophosphate ($\text{Na}_4\text{P}_2\text{O}_7$) precursors in 400 mL of deionized water (Solution B). Solution B was prepared with different molar ratios of orthophosphate and pyrophosphate ions ($\text{PO}_4^{3-}/(\text{P}_2\text{O}_7^{4-} + \text{PO}_4^{3-})$), in order to study the influence of this parameter on the nature and composition of the final material. Samples are labelled NaPYG-0X0, from the lowest ($X = 0$) to the highest ($X = 6$) ortho/pyrophosphate ratio (Table 1). Solution A was then added to solution B using a peristaltic pump at a constant volumetric flowrate ($32 \text{ mL} \cdot \text{min}^{-1}$) for all samples. The mixture turned transparent to translucent. After complete addition, the solution was stirred for 5 more minutes (aliquots of the solution were collected during this step in order to measure the pH), and the final colloidal solution was centrifuged 5 minutes at 7500 rpm. The resulting dense gel at the bottom of the centrifuge tube was washed three times with deionized water. Finally, the washed gel was poured into a glass crystallizing dish and dried at 70°C during 7 days. Samples were then stored at -20°C before their characterization (carried out at ambient temperature).

α -canaphite ($\text{Na}_2\text{CaP}_2\text{O}_7 \cdot 4\text{H}_2\text{O}$) and nanocrystalline apatite were prepared for use as reference compounds for Raman spectroscopy, XRD, and solid state NMR characterizations, because they were

occasionally identified in some of the final materials. The nanocrystalline apatite reference sample was synthesized according to a previously published protocol [27]. The canaphite reference sample was prepared by adapting the protocol reported by Cheng *et al* [28] (SI-1). These two reference samples were characterized by solid state NMR and Raman spectroscopy and XRD, and were demonstrated to be pure compounds.

Characterization

The synthesized materials were characterized using complementary structural, microstructural, elemental, spectroscopic and thermal characterization methods.

Powder X-ray diffraction analysis was performed using a diffractometer (Bruker D8 advanced) with a copper anticathode ($\lambda(K_{\alpha 1}) = 1.54056 \text{ \AA}$, $\lambda(K_{\alpha 2}) = 1.54433 \text{ \AA}$), stepsize of 0.03° between 10° and 70° . Samples were crushed without sieving in a mortar before measurements.

Magic-angle spinning (MAS) solid state NMR experiments were performed to analyze ^{31}P , ^{23}Na , ^1H and ^{43}Ca local environments in the materials. ^1H single pulse, ^{23}Na single pulse, ^{31}P single pulse, $^1\text{H} \rightarrow ^{31}\text{P}$ CP (Cross-Polarization) and ^{31}P CP INADEQUATE [29] (Incredible Natural Abundance Double QUAntum Transfer Experiment) spectra were recorded on a VNMRS-600 MHz (14.1 T) instrument equipped with a Varian T3 3.2 mm triple resonance probe using 14 to 20 kHz spinning speeds. ^1H single pulse and ^1H Hahn echo spectra were acquired at 14.1 T using a Varian 1.2 mm triple resonance probe spinning at 40 kHz. $^1\text{H}\{^{31}\text{P}\}$ HETCOR (HETeronuclear CORrelation) spectra and additional ^1H Hahn-echo experiments were also recorded at 14.1 T using a 1.6 mm triple resonance probe, with 22 to 30 kHz spinning speeds. ^{31}P CP SQ-DQ (Single Quantum-Double Quantum) experiments with SPC5 recoupling were performed on a 700 MHz (16.4 T) Bruker AVANCE III spectrometer, equipped with a 4 mm double resonance MAS probe spinning at 14 kHz [30]. The $^{23}\text{Na}\{^{31}\text{P}\}$ D-HMQC (Heteronuclear Multiple-Quantum Correlation) [31] spectra were acquired on a 800 MHz Bruker Advance NEO 4 spectrometer (18.8 T) equipped with a 3.2 mm HXY MAS probe using 20 kHz spinning speed. ^{43}Ca multi-DFS (Double Frequency Sweep) NMR [32] spectra were acquired on a 850 MHz Bruker NEO 4 spectrometer (20.0 T), a 800 MHz Bruker advance NEO spectrometer (18.8 T), or the 35.2 T SCH magnet in Tallahassee (FL-USA, using a Bruker AVANCE NEO console), respectively equipped with a 7 mm X low gamma probe, a 4 mm HX Tallahassee probe and a 3.2 mm MAS Tallahassee probe using

5 to 10 kHz spinning speed [33,34]. The complete set of acquisition parameters can be found in supporting information (SI-2), including information on temperature regulation and the referencing of spectra, and a table with all acquisition parameters (Table S1).

Raman scattering analyses were performed using a Raman Labram HR 800 confocal microscope Horiba Yvon Jobin. The sample was exposed to continuous laser radiation provided by a 532 nm Argon diode laser with a power of 14 mW. The analyses were carried out under a BX 41 Olympus microscope equipped with a x100 lens with a numerical aperture of 0.9, which confers to the system a lateral resolution of 1.0 μm and an axial resolution of 4.5 μm . The spectrum of each microdomain was acquired through a grating of 600 lines per mm with a spectral resolution of 1.5 cm^{-1} and collected with a quantum well detector cooled at $-60\text{ }^{\circ}\text{C}$ by double Peltier effect (CCD Synapse). A certified silicon standard was used to calibrate the frequency of the equipment using the first order silicon line at 520.7 cm^{-1} . Each spectrum was acquired with an integration time of 30 seconds and 5 accumulations. The methodology for Raman lines decomposition to evaluate the ortho/pyrophosphate ratio in the synthesized materials is described in the Supporting Information (SI-3, Table S2).

Scanning Electron Microscopy (SEM) analyses were performed on a LEO 435 VP microscope with an accelerating voltage in the 8-12 kV range. Except for NaPYG-000, all samples were crushed in a mortar until getting submillimetric grains (without sieving) that were stuck on adhesive carbon discs and finally silver sputter-coated before observation.

Thermogravimetric Analyses (TGA) and Differential Thermal Analysis (DTA) were performed using a Setaram instrument (Setsys Evolution System) from 25 to 600°C with a stage of 20 min at 600°C , and a heating rate of 4°C per minute in air flow.

Inductively Coupled Plasma-Optical Emission Spectrometry ICP-OES (Ultima Expert machine) was used to analyze solutions of dissolved powders in order to determine the Ca, P and Na contents in the materials ($\lambda_{\text{Ca}} = 318.12\text{ nm}$, $\lambda_{\text{P}} = 177.43\text{ nm}$, $\lambda_{\text{Na}} = 589.59\text{ nm}$).

Ultra High Pressure Phase Liquid Chromatography (UHPLC) coupled with an Evaporative Light Scattering Detector (ELSD) was used for the detection of chloride ions (using a Waters Acquity apparatus). The analyzed solutions were the same as for ICP-OES spectrometry analysis. Standard calibration solutions were used (with $[\text{Cl}^-]$ from 0 to 1.5 ppm).

Statistics and errors

Uncertainties in Table 1 are due to volume, mass and pH measurement errors and subsequent propagation of uncertainty. Uncertainties in pyrophosphate, orthophosphate (Table 2 and Figure 7) calcium, phosphorus and sodium (Table 3) quantification correspond to the standard deviation (triplicate) determined on values obtained by Raman and NMR spectra deconvolution and ICP measurements. Uncertainty associated to water quantification (Table 3) is the nominal value associated to the TGA apparatus. Those associated to the final composition, charges and the corresponding summations (Figure 5) have been calculated by the propagation of uncertainty with previous results.

Results

1) Morphology

Seven calcium phosphate materials (NaPYG-000 to NaPYG-060) were prepared in water under mild conditions, using a fixed amount of Ca^{2+} and different molar ratios of ortho and pyrophosphate entities: $\text{PO}_4^{3-}/(\text{P}_2\text{O}_7^{4-} + \text{PO}_4^{3-})$ (Table 1). Although the synthesized materials were obtained as powders for all synthesis conditions, they appeared visually different: a fine powder was observed for NaPYG-000 (prepared from only pyrophosphate precursor solution), whereas grains of several millimeters size with mechanical cohesion were observed for the other compositions (prepared from mixed ortho and pyrophosphate precursor solutions). Scanning Electron Microscopy observations (Figure 1) show that: NaPYG-000 is composed of grains with diameters between 20 and 100 μm . These grains are either spherulites or bundles formed by plate-like crystals of around 2 μm width and 0.5 μm thickness. For the other samples, after grinding, the particles appear to have angular shapes, with smooth and compact fracture surfaces with irregular morphologies. These conchoidal fractures are typical of brittle materials [35]. Figure 1 (j, k, l) shows an increase in the submicronic surface roughness, associated with an increase of the initial ortho/pyrophosphate molar ratio in solution (from NaPYG-010 to NaPYG-060).

2) Structural analyses

The nature of the phases involved was determined by X-ray diffraction analysis (Figure 2-a). Samples NaPYG-010 to 050, prepared from solutions containing both pyro- and orthophosphates, were

found to be amorphous (very broad halo between 26° and 34°). On the contrary, well-defined crystalline peaks were observed for NaPYG-000. These peaks were identified as those of α -canaphite [36], $\text{Na}_2\text{CaP}_2\text{O}_7 \cdot 4\text{H}_2\text{O}$. X-ray diffractogram of NaPYG-060, showed features of a nanocrystalline apatite [18], although the apparent crystallite sizes (length and thickness) should be different than that of the nanocrystalline apatite reference sample (3 days of maturation, non-carbonated). Indeed, L(200) (giving information on the length of apatite nanocrystals) and L(310) (giving information on the thickness of apatite nanocrystals) have been calculated using Scherrer's law. These values are respectively: $L(200)_{\text{ref}} = 17.2 \pm 0.6 \text{ nm}$, $L(310)_{\text{ref}} = 8.3 \pm 0.6 \text{ nm}$, $L(200)_{\text{NaPYG060}} = 29.2 \pm 0.6 \text{ nm}$, $L(310)_{\text{NaPYG060}} = 9.2 \pm 0.6 \text{ nm}$.

For NaPYG materials, six main domains in the corresponding Raman spectra (Figure 2-b) could be distinguished for the phosphate/pyrophosphate entities [16]:

- i) One domain between 410 - 650 cm^{-1} corresponding to vibrational bands of both orthophosphate and pyrophosphate ions (δPO_3 and ρPO_3 of P_2O_7 and $\nu_4\text{PO}_4$).
- ii) Four domains assigned to the pyrophosphate entities only, including the bending mode of the POP bridge (δPOP) around 350 cm^{-1} ; the symmetric stretching of POP ($\nu^s\text{POP}$, between 695 and 795 cm^{-1}) and the intense lines of $\nu^s\text{PO}_3$, between 1015 and 1070 cm^{-1} and of $\nu^{\text{as}}\text{PO}_3$ between 1080 and 1195 cm^{-1} .
- iii) One domain corresponding mainly to the symmetric stretching of orthophosphate entities ($\nu^s\text{PO}_4$) between 915 and 990 cm^{-1} .

For NaPYG-000 and NaPYG-060, only the bands associated with pyrophosphate or orthophosphate ions were observed, respectively, as expected. Moreover, these bands, especially $\nu^s\text{PO}_3$ (orthophosphate) and $\nu^s\text{PO}_4$ (pyrophosphate) were found to be narrower ($\text{FWHM}_{000} = 13 \text{ cm}^{-1}$ and $\text{FWHM}_{060} = 13 \text{ cm}^{-1}$) than for other compositions. It indicates the predominant presence of well-defined environments belonging to crystalline phases, matching with α -canaphite ($\text{FWHM}_{\text{pyro}} = 10 \text{ cm}^{-1}$) for NaPYG-000 and nanocrystalline apatite ($\text{FWHM}_{\text{ortho}} = 12 \text{ cm}^{-1}$) for NaPYG-060. For the other compositions, broad lines typical of amorphous phases ($\text{FWHM}_{\text{pyro}} = 25\text{-}29 \text{ cm}^{-1}$ and $\text{FWHM}_{\text{ortho}} = 26\text{-}29 \text{ cm}^{-1}$) were observed. Considering the $\nu^s\text{PO}_4$ band of the orthophosphate ion at 955 cm^{-1} , its intensity was found to increase, as expected, with the increase in the relative proportion of orthophosphate ions in the initial solution (from NaPYG-010 to NaPYG-050). This trend is opposite for the pyrophosphate stretching band ($\nu^s\text{PO}_3$ at 1038 cm^{-1}), showing a decrease in the pyrophosphate when the orthophosphate/pyrophosphate ratio in the synthesis solution was increased (Table 2).

^{31}P MAS solid state NMR spectra were recorded in order to analyze more accurately the environments of ortho- and pyrophosphate anions. First, using single-pulse excitation experiments in quantitative mode, the general trends observed in Raman spectroscopy were confirmed (Figure 3-a). Indeed, two regions were observed on the spectra, which correspond predominantly to the different types of phosphate units, based on previous NMR studies [16,17] and on additional ^{31}P CP-INADEQUATE (discrimination of pyrophosphate entities) experiments (see Supporting Information, SI-4, Figure S1):

- i) between 8 and -1 ppm mainly for orthophosphate species,
- ii) between -2 and -10 ppm for pyrophosphate species

For NaPYG-000 and NaPYG-060, narrow resonances were observed, which were respectively attributed to the pyrophosphate environment of α -canaphite (-2.5 and -5.8 ppm) and orthophosphate environment of nanocrystalline apatite (2.8 ppm). However, it is worth noting that in the case of NaPYG-000, a broad underlying component due to pyrophosphate environment was also observed, accounting for $\sim 23\%$ of the overall phosphorus intensity. This implies that NaPYG-000 also contains an amorphous component (in addition to α -canaphite). For samples NaPYG-010 to NaPYG-050, broad resonances were observed, as expected for amorphous materials. Their relative intensity was found to vary in the same way as the proportion of orthophosphate versus pyrophosphate species in the initial precursor solution, in line with Raman spectroscopic analyses (Table 2). $^1\text{H} \rightarrow ^{31}\text{P}$ CP-MAS experiments were also carried out on all samples (SI-4, Figure S1), showing that both types of phosphate units are in close proximity to protons, which belong mainly to water molecules (main resonance on the ^1H MAS NMR spectra of all compounds, centered at ~ 5 ppm, Figure 3-c). A similar observation was made in the case of amorphous potassium ortho/pyrophosphate materials [17]. A more complete discussion of the ^1H and ^{31}P environments is given later in this manuscript.

The local environments of Na^+ and Ca^{2+} cations were also probed using solid state NMR. Regarding ^{23}Na MAS NMR data, all samples were analyzed at two different magnetic fields, to ensure a sounder interpretation of the data, as ^{23}Na is a spin 3/2 quadrupolar nucleus (Figure 3-b, and supporting information SI-5). NaPYG-000 showed two distinct Na environments with well-defined second-order quadrupolar lineshapes (as expected from the crystal structure of α -canaphite [36], see Figure S4). However, no broad ^{23}Na resonance related to the amorphous ^{31}P was observed, suggesting the presence of an amorphous calcium pyrophosphate. On the other hand, NaPYG-060 showed a narrow and yet

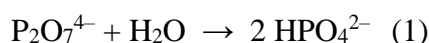
slightly distributed Na environment, which corresponds to Na⁺-substitutions in nanocrystalline apatite [37]. For samples NaPYG-010 to NaPYG-050, a broad asymmetric resonance was observed in all cases, with a tailing towards the lower frequencies. Spectral deconvolutions of these samples were performed considering the presence of two distinct Na environments (see SI-5, Figure S3 and Table S3), as no satisfactory fit could be achieved using a single one. The relative proportion between both components did not appear to vary significantly with the ortho/pyrophosphate ratio, and remained equal to ~20/80 along the series. The narrowest ²³Na resonance could correspond to Na⁺ ions which are in a more symmetric and/or more mobile environment due to a higher amount of water molecules in their vicinity.

Concerning ⁴³Ca MAS NMR, all analyses were performed at ultra-high field ($B_0 \geq 18.8$ T), as ⁴³Ca is a spin 7/2 quadrupolar nucleus of low resonance frequency and with a natural abundance of only 0.14% (Figure 3-d). All ⁴³Ca NMR spectra showed a broad resonance centered at ~ 0 ppm. Based on the comparison of the data recorded at 20.0 and 35.2 T (see SI-6, Figure S5), and on previous ⁴³Ca NMR studies of amorphous Ca-(pyro)phosphate phases, the breadth of these signals mainly attests of a chemical shift distribution, possibly caused by distributions in Ca-O bond distance variations [34,38,39]. For two samples (NaPYG-010 and NaPYG-050), an additional distinct environment was also visible, with an underlying component at the lower frequencies (Figure 3-d). However, due to the difficulties in recording such spectra at natural abundance, and despite the use of signal-enhancement schemes, no exact quantification of this component was accessible at this stage. Taken together, ²³Na and ⁴³Ca NMR analyses underscore the complex nature of the amorphous NaPYG-010 to NaPYG-050 materials, in which not only two different types of anions are present (ortho and pyrophosphates), but also a variety of cation environments.

3) Thermal behavior and chemical compositions

The thermal evolution of the NaPYG samples was studied by TGA-DTA. Figure 4 shows the TGA and DTA curves of NaPYG-000, NaPYG-010, NaPYG-030 and NaPYG-060. Only four samples are presented for the ease of reading, since the curves were very similar for samples NaPYG-020, NaPYG-040 and NaPYG-050 (see SI-7, Figure S6). The weight losses of water for all the synthesized materials are reported in Figure 4 and summarized in Table 3. These weight losses can be due to the release of water which is either adsorbed, directly involved in the bulk structure of these materials or

resulting from P-OH condensation. For NaPYG-000 (which contains a significant amount of crystalline α -canaphite), the main weight loss (~16%) appeared at fairly low temperatures (between 80°C and 170°C), and was associated with an important endothermic event. The final weight loss was below the theoretical value expected for the loss of the four water molecules (21.6%) involved in α -canaphite ($\text{Na}_2\text{CaP}_2\text{O}_7 \cdot 4\text{H}_2\text{O}$), and consistent with the loss of three water molecules. The missing water molecules could be due to the remaining amorphous component part for which the hydration rate can be different from the crystalline part. They could also be involved in the internal hydrolysis of part of pyrophosphate ions into orthophosphate ones (Equation (1)), associated with a small exothermic contribution around 173°C (SI-7, Figure S6). Such a phenomenon has been reported in other hydrated calcium pyrophosphates [15,16].



Finally, the peak at 433°C corresponds to the crystallization of anhydrous $\text{Na}_2\text{CaP}_2\text{O}_7$ phase (XRD data not shown). The general aspect of the weight loss curves was found to be quite similar for the amorphous samples NaPYG-020 to NaPYG-050 (see SI-7, Figure S6), with final percentage losses between 12 and 16%. All showed broad endothermic peaks attributed to water release (between 50 and 190°C). In contrast, a first plateau was observed for NaPYG-010 (at ~194°C), corresponding to a slowdown of water loss. This plateau was probably due to an internal hydrolysis (associated with an exothermic peak around 173°C) as water molecules are involved in this reaction. It is not observed for the other amorphous samples probably due to their lower initial pyrophosphate amount. An endothermic event associated to this plateau then occurred (from ~220°C) due to the quick loss of H_2O after hydrolysis. For NaPYG-060 (nanocrystalline apatite), the weight loss was continuous (dehydration) up to 600°C, with a total weight loss below 5%. This value is consistent with those of nanocrystalline apatites (between 4 and 10%) [40].

Ca, Na and P amounts in NaPYG-0X0 materials were measured by ICP-OES spectrometry, after dissolution of the materials. Results were used to extrapolate the number of moles of each of these elements in 100 g of material (see Table 3 and supporting information SI-8 for the %). UHPLC was used to quantify chloride ions after dissolution: for all NaPYG material compositions, chloride concentrations were found to be below the detection limit, i.e. 10^{-6} mol of Cl^- for 100 g of material. For NaPYG-060 the concentrations of Ca, P and Na were consistent with Na-substituted nanocrystalline

apatite [41]. For NaPYG-000, these values were found to be comparable to those of canaphite ($\text{Ca/P} = 0.5$ and $\text{Ca/Na} = 0.5$): $(\text{Ca/P})_{\text{exp}} = 0.541$ and $(\text{Ca/Na})_{\text{exp}} = 0.548$. The difference can be attributed to the presence of the amorphous phase as shown by ^{31}P MAS NMR. For the other samples (amorphous), Ca amount increased with the ortho/pyrophosphate ratio from NaPYG-010 to NaPYG-040 and slightly decreased for NaPYG-050. At the same time, the phosphorus and sodium proportions decreased. These interdependent evolutions of calcium, sodium and phosphorus will be further discussed below.

Discussion

1) Texture and composition of the amorphous NaPYG materials

Considering SEM observations (Figure 1) at the lowest magnification, the morphologies of the materials containing mixed ortho/pyrophosphate entities (NaPYG-010 to NaPYG-050) were similar to those observed for sol-gel derived silica or bioactive silicate glasses [42]. Indeed, without taking any particular precaution during the gel drying step, a powder was observed with angular shapes, smooth compact surfaces, and irregular fractures due to solvent evaporation. This was the case for all amorphous NaPYG materials, contrary to NaPYG-000 for which the size of powder grains seemed essentially related to the crystallite size of the α -canaphite component. Conventional sol-gel processes involving silicon alkoxide precursors [43], colloidal gels are formed (at basic pH), leading to materials composed either of aggregated colloids when drying at moderate temperatures, or of a continuous network of coalesced particles (depending on the temperature of the final thermal treatment). Although this conventional sol-gel method was not implemented in the present study, preliminary TEM measurements were performed on NaPYG-030 materials (SI-9, Figure 7), suggesting that the millimetric grains of amorphous NaPYG materials were not formed of a continuous network but by the aggregation of colloids/nanoparticles (with a diameter from a few nanometers to several dozens of nanometers with a hierarchical organization). Considering the large amount of remaining water (between 12 and 16 w%), one could suggest that part of it is due to non-structural water located in the inter-colloidal spaces. Although it has not been demonstrated, it may play a key role in the material cohesion as the hydrated layer at the surface of apatite nanocrystals [44].

The relative proportions of phosphorus atoms involved as pyrophosphate ($\%P_{\text{pyro}}$) and orthophosphate ($\%P_{\text{ortho}}$) species were determined by fitting the ^{31}P solid state NMR and Raman spectroscopic data (methodology for Raman in SI-3, Table S2). These results (Table 2) were compared to the proportions $\%P_{\text{pyro}}$ and $\%P_{\text{ortho}}$ in the initial solutions. First, it should be noted that similar values were found by ^{31}P NMR for materials of different synthetic batches corresponding to the same targeted composition, showing the reproducibility of these syntheses (SI-10). Second, Raman and NMR quantifications were found to be consistent with each other (maximum difference of 7%). The small variations between both quantifications could be due to slight differences in the Raman scattering coefficients of respective orthophosphate and pyrophosphate bands (SI-3). The percentages of each phosphate species in the amorphous solids were found to globally follow the same trend as in the phosphate precursor solutions, i.e. a progressive increase of orthophosphates from NaPYG-010 to NaPYG-050, at the expense of pyrophosphates (non-linearity of evolution and excess of orthophosphates are discussed below). Combining these results with those of ICP-OES spectrometry and TGA, weight percentage of Ca^{2+} , Na^+ , PO_4^{3-} , $\text{P}_2\text{O}_7^{4-}$ ions and H_2O have been calculated for each composition. All weight percentages are reported in Figure 5-a (and SI-8, Table S4). The calcium and orthophosphate amounts were found to be clearly correlated, and to increase from NaPYG-010 to NaPYG-050 for orthophosphates and from NaPYG-010 to NaPYG-040 for Ca^{2+} ions. Simultaneously, sodium and pyrophosphate contents decreased.

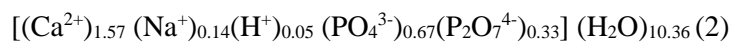
The ionic charge balance was determined (per 100 g of sample) for each composition. As a first assumption, ortho- and pyrophosphate ions were considered as non-protonated in these calculations (Figure 5-b). They demonstrate that the relative value of the charge of phosphate species decreases when the relative amount of orthophosphates increases. The calcium charge evolution has the opposite curve trend to compensate it. Calcium is then the main counter-ion of phosphate species. It can be considered as a “linker” maintaining the cohesion of the phosphate network in these materials. Sodium, however, appears to only act as a positive “calcium substitute” when the amount of the latter is not high enough to balance the phosphate negative charges (NaPYG-010 and NaPYG-020). This effect of the local electric field should be predominant in absence of any additional steric effect as both cations have similar ionic radius (116 pm for Na^+ and 114 pm for Ca^{2+} , respectively). The sum of charges is still slightly negative and decreases with the amount of orthophosphate ions as previously indicated, suggesting an

increase of protonation of phosphate entities. Considering this hypothesis, the calculated protonation rate of P-O groups are low and varies from 1.0% (NaPYG-010) to 3.6% (NaPYG-050) whatever the phosphate species (ortho/pyrophosphate).

Additional ^1H solid state NMR analyses were thus carried out to investigate in more detail the protonation of the phosphate groups. While single pulse experiments essentially showed one main resonance corresponding to water molecules (Figure 3-c), Hahn echo experiments revealed the presence of underlying signals at higher chemical shifts (> 8 ppm) (Figure 6-a), which are consistent with protonated phosphates [45]. Additional $^1\text{H} \rightarrow ^{31}\text{P}$ HETCOR experiments were performed, which revealed correlations between these additional ^1H resonances and the ortho and pyrophosphate ^{31}P peaks at short contact times, thereby confirming their assignment to P-OH species (Figure 6-b and SI-11, Figures S9 and S10). Pyrophosphate are overall less protonated than orthophosphate. At this stage, a general chemical formula (Formula 1) can be proposed by combining ^{31}P solid state NMR, ICP-OES spectrometry and TGA (assuming that the sum of orthophosphate and pyrophosphate equals to 1):



The stoichiometric coefficient of H^+ was not measured but calculated considering the neutrality of the compound. In the case of NaPYG-030 for example, we determined that the chemical formula (Formula 2) is:



In such materials orthophosphates and pyrophosphates can be considered as forming entities of the network whereas Ca^{2+} are bridging bivalent cations between phosphate species (pyro- and/or orthophosphates) and Na^+/H^+ non-bridging cations. As stated in our previous work [17], such compositions are close to those of invert glasses [46,47], that are elaborated by fusion with high amounts of glass modifying oxide (CaO) compared to forming oxide (P_2O_5). However, contrary to invert glasses, NaPYG materials contain a high amount of water and no clear glass transition temperature (T_g) was observed in thermal analyses. Hydrated amorphous calcium pyro- or orthophosphates synthesized at ambient temperature have also been described [10,15], but without both phosphate entities (or with small amount of orthophosphate generated *in situ* [16]).

2) Control of the ortho/pyrophosphate ratio and mechanism of formation of NaPYG materials

The formation of amorphous NaPYG materials is allowed by the inhibitory effect of orthophosphate ions on calcium pyrophosphate phase crystallization (and reciprocally) as illustrated by the data (NaPYG crystalline samples resulting from solutions containing only ortho- or pyrophosphate and amorphous samples resulting from solutions containing both phosphate species) and already described in the literature [47,48,49]. The possibility to finely control the pyro/orthophosphate ratio from the initial solution to give amorphous materials is particularly interesting in a view of biomedical applications to potentially reach tunable degradation due to pyrophosphate hydrolysis. Figure 7 presents the evolution of % $P_{\text{orthophosphate}}$ (vs % $P_{\text{pyrophosphate}}$) in NaPYG materials as a function of the initial % $P_{\text{orthophosphate}}$ in the precursor solution. ^{31}P solid state NMR and Raman spectra evolutions showed the same trend: % $P_{\text{orthophosphate}}$ in the materials are higher than those of the precursor solution for materials synthesized with solutions rich in pyrophosphate entities (NaPYG-010/020/030), becoming closer in the case of orthophosphate rich solutions (NaPYG-040/050). Several hypotheses can be proposed to explain this orthophosphates overconcentration in the final material compared to pyrophosphates.

The first explanation is a partial hydrolysis of pyrophosphates into orthophosphates for low initial ortho/pyrophosphate ratios. Considering the basic pH of all the solutions (Table 1), this hydrolysis reaction is unlikely to occur during the first steps (colloidal solution and gel) [16] However, a solid state hydrolysis may occur during the drying step at 70°C. This assertion is supported by the fact that stronger correlations are observed on the ^1H - ^{31}P HETCOR spectra between the P-OH groups and the orthophosphate ^{31}P resonances (rather than the pyrophosphate ones) (see Figure 6-b). Nevertheless, the protonation rates of P-O groups calculated above (1.0% - 3.6%) are too low to explain the overconcentration of orthophosphate.

The second explanation could be linked to the mechanism of colloids formation in the solution and the preferential association of orthophosphate with calcium (vs pyrophosphate). Here, this would imply two different possibilities: **i**) orthophosphate and pyrophosphate ions are segregated into two different entities (ions pair, clusters...) and the solubility of the first one is higher leading to higher orthophosphate amount in the final material. Unfortunately, the pK of such amorphous entities has been poorly described, preventing the (in)validation of this hypothesis, **ii**) colloids are formed of entities associating both pyrophosphate and orthophosphate ions, the latter being predominant due to charges

equilibrium. The results obtained for non-washed samples could confirm the segregation. Indeed, without any washing of the gel, canaphite was mainly formed for NaPYG-010, and nanocrystalline apatite for NaPYG-050, while a mix of both was observed for NaPYG-030 (SI-12). This is a proof that two kinds of nuclei are formed in the solution either containing orthophosphate or pyrophosphate. Moreover, it demonstrates that the washing step is critical to form amorphous materials, by removing remaining ions (not involved in the nuclei) from the gel.

Beyond the colloidal solution, one might wonder if the phosphate ions are still segregated in amorphous materials and how they are structured or associated. For this purpose, amorphous NaPYG could be compared to amorphous calcium (ortho)phosphates (ACPs) [10] for which the most common theory considers they are formed by building blocks called Posner's cluster [50]. These clusters are around 1 nm in diameter and have a core chemical composition of $\text{Ca}_9(\text{PO}_4)_6$ and a well-defined structure [51]. These units have been identified in the first steps of hydroxyapatite and several other crystalline calcium orthophosphates formation [52]. Analogous cluster models of amorphous Ca-pyrophosphates have not been described to date. However, previous PDF (pair distribution function) studies [15,53] on hydrated and amorphous pyrophosphate phases ($\text{Ca}_2\text{P}_2\text{O}_7 \cdot n\text{H}_2\text{O}$) demonstrated a complete loss of structural coherence beyond interatomic separations greater than 7.5-8.0 Å that can be attributed to calcium pyrophosphate clusters.

Additional high resolution solid state NMR experiments were performed to analyze in more detail the nature of the domains forming the NaPYG amorphous materials. First, a ^{31}P SQ-DQ NMR experiment was performed, which allows probing the proximities between ortho- and pyrophosphate units (Figure 8-a). The observation of cross peaks on the 2D spectrum is a proof of the spatial proximity between ortho- and pyrophosphate units. Second, ^{23}Na - ^{31}P D-HMQC experiments were performed (Figure 8-b), in order to probe the Na^+ /phosphate proximities. The same correlation was observed between the broad ^{23}Na resonance and the two types of phosphate units, which further confirms that these anions are intimately associated in the material. While both of these NMR experiments demonstrate the existence of mixed ortho-/pyrophosphate entities, the additional presence of some segregated ortho- or pyrophosphate domains/clusters cannot be ruled out at this stage.

The charge compensation within clusters is meant to be ensured by both Ca^{2+} and Na^+ ions. A recent molecular dynamics study [54] has shown that the stoichiometry of orthophosphate clusters can

slightly vary depending on several parameters such as ageing of the solution, protonation of phosphate groups, partial calcium substitution by sodium ions, variation of supersaturation ratios. When orthophosphates are partially protonated, sodium was shown to be a substitute for calcium in the external layer of the Posner-like clusters, with various Na/Ca ratios. Another recent study has demonstrated that sodium could facilitate the aggregation of charged clusters and could substitute for calcium as cluster-binding cation [55]. Based on these studies, a hypothesis of mixed ortho/pyrophosphates cluster can be proposed explaining the ^{23}Na NMR data (Figure 3-d). Indeed, the two Na^+ environments which were detected could correspond to intra-cluster sodium sites (broad signal which correlates to the ortho and pyrophosphate signals) and more mobile sodium ions at the surface of these clusters. Naturally such hypothesis will need to be confirmed by complementary investigations (coupled WAXS/SAXS associated with simulation).

Conclusion

This article describes the low temperature synthesis of hydrated amorphous calcium/sodium ortho-/pyrophosphate materials (NaPYG). For the first time, these compounds were obtained in a large range of orthophosphate/pyrophosphate molar ratios, mainly due to reciprocal inhibitory effect of the two phosphate entities on their respective crystallization with calcium. This ratio can be controlled in the final material as its evolution follows the same trend than that of phosphate precursors in the initial solution (with orthophosphates in excess in the amorphous materials). Controlling this ratio is of major interest as it could open the way for the tuning of enzyme or pH-driven degradation rate of such materials.

Preliminary results regarding the behavior of the samples *in vitro* have been obtained, revealing that : i) the pyrophosphates could be hydrolyzed in water, in standard SBF solutions and in TRIS media supplemented or not with ALP enzymes ii) the evolutions of the different materials are correlated with their initial ortho/pyro-phosphate ratio. Clearly this ratio appears as a key parameter potentially offering the ability to tune up the biological behaviour. The complete *in vitro and in vivo* study of these materials will be presented in a forthcoming publication. Beyond their synthesis, multi-scale characterizations have been carried out, including advanced multinuclear solid state NMR. This led to a general formula

quantifying their composition. The data suggest that these solids are formed by the aggregation of colloids. They are also consistent with a cluster-based material. Although their existence will need to be investigated in detail by complementary techniques, such clusters could be formed by calcium, sodium and partially protonated ortho- and pyrophosphate entities and be associated together through surface water and sodium cations, ensuring the overall cohesion of the whole material.

Supporting information

SI-1: Synthesis of α -canaphite

SI-2: Full experimental details of the solid state NMR experiments.

SI-3: Methodology for the determination of the orthophosphate and pyrophosphate proportions from Raman spectra

SI-4: ^{31}P CP-INADEQUATE and CP-MAS solid state NMR spectra

SI-5: ^{23}Na solid state NMR data, including spectral deconvolutions

SI-6: ^{43}Ca solid state NMR data of NaPYG-050, recorded at both 20.0 T and 35.2 T.

SI-7: TGA and DTA of NaPYG-020, NaPYG-030, NaPYG-040, NaPYG-050 samples.

SI-8: Mass percentages of Ca^{2+} , Na^+ , PO_4^{3-} , $\text{P}_2\text{O}_7^{4-}$ and H_2O in NaPYG materials.

SI-9: TEM picture of NaPYG030 sample.

SI-10: Comparison of ^{31}P and ^{23}Na NMR spectra of materials from different synthetic batches of NaPYG-010.

SI-11: ^1H Hahn echo spectra of NaPYG materials, and $^1\text{H} \rightarrow ^{31}\text{P}$ HETCOR study of NaPYG-010.

SI-12: XRD diagrams and Raman spectra of NaPYG materials obtained without the washing step.

Acknowledgments

The authors would like to thank the Agence Nationale de la Recherche (PyVerres project - grant n°ANR-16-CE19-0013) for supporting this research work. The authors are grateful for access to UK 850 MHz solid-state NMR Facility used in this research and funded by EPSRC and BBSRC (contract reference PR140003), as well as University of Warwick including via part funding through Birmingham Science City Advanced Materials Project 1 and 2, supported by Advantage West Midlands (AWM) and the European Regional Development Fund (ERDF). A portion of this work was performed at the National High Magnetic Field Laboratory, which is supported by the National Science Foundation Cooperative Agreement No. DMR-1157490 & DMR-1644779, and the State of Florida. The French Région Ile de France - SESAME program is acknowledged for financial support (700 MHz NMR spectrometer). Dinu Iuga isacknowledged for their assistance in some of the NMR experiments.

Conflicts of interest

There are no conflicts to declare.

Figure captions list

Figure 1: SEM micrographs of synthesized NaPYG materials at different magnifications: NaPYG-000 (a, e, i), NaPYG-010 (b, f, j), NaPYG-030 (c, g, k) and NaPYG-060 (d, h, l).

Figure 2: (a) XRD patterns and (b) Raman spectra of NaPYG materials prepared with different ortho/pyrophosphate molar ratios: from NaPYG-000 (top) to NaPYG-060 (bottom). Results for the synthesized canaphite and nanocrystalline apatite reference samples are also presented for comparison. (see supporting information).

Figure 3. a) ^{31}P single pulse MAS NMR spectra recorded at 14.1 T, using $\nu_r = 14$ kHz. b) ^{23}Na single pulse MAS NMR spectra recorded at 14.1 T using $\nu_r = 20$ kHz. c) ^1H single pulse MAS NMR spectra recorded at 14.1 T using $\nu_r = 40$ kHz. d) ^{43}Ca multi-DFS MAS NMR spectra recorded at 18.8 or 20.0 T using $\nu_r = 4\text{-}6$ kHz. Full details on the acquisition conditions are provided in Supporting Information (SI-2).

Figure 4. (a) TGA and (b) DTA curves for NaPYG-000, NaPYG-010, NaPYG-030, NaPYG-060 materials. An expansion of the DTA curves is given in Figure S6-c.

Figure 5. (a) Evolution of weight percentages of Ca^{2+} , Na^+ , PO_4^{3-} , $\text{P}_2\text{O}_7^{4-}$, H_2O , and summation of all these ions and (b) Evolution of charges (number of moles of each ionic entity for 100 g of material normalized by its respective charge) for calcium, sodium, total phosphate and summation for each amorphous NaPYG material (x axis is the percentage of $\text{P}_{\text{orthophosphate}}$ with respect to the total phosphorus content).

Figure 6. a) ^1H Hahn echo MAS NMR spectra of NaPYG-010 material recorded at 14.1 T, spinning at 22 kHz, using different echo delays ($\tau = 33, 133$ and $533 \mu\text{s}$), showing the presence of protonated phosphate resonances at higher chemical shifts (> 8 ppm); b) $^1\text{H} \rightarrow ^{31}\text{P}$ HETCOR NMR spectrum of NaPYG-010 recorded at 14.1 T, spinning at 22 kHz and using a short contact time (0.1 ms). The ^1H Hahn echo spectrum recorded with $\tau = 533 \mu\text{s}$ is shown on the ^1H projection of the HETCOR. The ^1H NMR spectra in blue and red correspond to the ^1H signals of the HETCOR which correlate with the pyro- and ortho-phosphate species, respectively.

Figure 7. Molar percentage of phosphorus atoms involved in orthophosphate ions (compared to pyrophosphate) in materials (as determined by solid state NMR and Raman spectroscopy) as a function of the molar percentage of orthophosphate ions in the initial precursor solution.

Figure 8. (a) ^{31}P SQ-DQ spectrum of NaPYG-030 acquired at 16.4 T, spinning at 14 kHz. The dashed red boxes show the cross-peaks between ortho and pyrophosphate units, (b) $^{23}\text{Na}^{31}\text{P}$ D-HMQC spectrum of NaPYG-010 material, acquired at 18.8 T using 20 kHz spinning speed (the ^{23}Na NMR spectra in blue and red correspond to correlations with pyro- and orthophosphate ions, respectively).

TABLES

Table 1: Number of moles of calcium and phosphate salt precursors involved in the initial solutions (A and B) and A and B solution volumes. Molar ratio, percentage, and pH after mixing the two solutions are also reported.

	NaPYG 000	NaPYG 010	NaPYG 020	NaPYG 030	NaPYG 040	NaPYG 050	NaPYG 060
CaCl ₂ ·2H ₂ O (mmol)	7.210 ± 0.020						
Na ₄ P ₂ O ₇ (mmol)	33.30 ± 0.008	28.300 ± 0.008	23.310 ± 0.008	16.650 ± 0.008	9.990 ± 0.008	4.990 ± 0.008	0
Na ₃ PO ₄ ·12H ₂ O (mmol)	0	4.990 ± 0.006	9.99 ± 0.005	16.65 ± 0.006	23.31 ± 0.006	28.30 ± 0.006	33.330 ± 0.006
Calcium solution (A) volume (mL)	40.0 ± 0.1						
Phosphate solution (B) volume (mL)	400.0 ± 0.1						
Ca/P (molar ratio)	0.109 ± 0.003	0.119 ± 0.004	0.128 ± 0.003	0.145 ± 0.003	0.166 ± 0.003	0.190 ± 0.004	0.220 ± 0.003
Orthophosphate initial molar %: PO ₄ ³⁻ /(P ₂ O ₇ ⁴⁻ + PO ₄ ³⁻)	0	15.00 ± 0.25	30.00 ± 0.14	50.00 ± 0.11	70.00 ± 0.12	85.00 ± 0.20	100
pH after mixing A and B solutions	10.1 ± 0.1	11.5 ± 0.1	11.8 ± 0.1	11.9 ± 0.1	12.0 ± 0.1	12.1 ± 0.1	12.1 ± 0.1

Table 2: Percentage of phosphorus atom involved in orthophosphate and pyrophosphate ions introduced as precursors in the initial solutions and in the final materials measured by ³¹P solid state NMR and Raman spectroscopy.

	Precursors in the initial solution		³¹ P solid state NMR of materials				Raman spectroscopy of materials			
	% P _{pyro}	% P _{ortho}	% P _{pyro}		% P _{ortho}		% P _{pyro}		% P _{ortho}	
NaPYG-000	100	0	100 ± 0	0 ± 0	100 ± 0	0 ± 0	100 ± 0	0 ± 0	0 ± 0	0 ± 0
NaPYG-010	92	8	74 ± 3	26 ± 3	67 ± 2	33 ± 2	67 ± 2	33 ± 2	67 ± 2	33 ± 2
NaPYG-020	82	18	58 ± 3	42 ± 3	52 ± 1	48 ± 1	52 ± 1	48 ± 1	52 ± 1	48 ± 1
NaPYG-030	67	33	50 ± 4	50 ± 4	47 ± 1	53 ± 1	47 ± 1	53 ± 1	47 ± 1	53 ± 1
NaPYG-040	46	54	37 ± 3	63 ± 3	37 ± 2	63 ± 2	37 ± 2	63 ± 2	37 ± 2	63 ± 2
NaPYG-050	26	74	26 ± 6	74 ± 6	31 ± 4	69 ± 4	31 ± 4	69 ± 4	31 ± 4	69 ± 4
NaPYG-060	0	100	0 ± 0	100 ± 0	0 ± 0	100 ± 0	0 ± 0	100 ± 0	0 ± 0	100 ± 0

Table 3: Chemical composition (Ca, P and Na) of the synthesized NaPYG materials determined by ICP-OES (moles/100 g of dissolved material) and total weight percent of water determined by TGA.

Samples	Ca (mol/100 g)	P (mol/100 g)	Na (mol/100 g)	H₂O w%
NaPYG-000	0.320 ± 0.003	0.591 ± 0.004	0.583 ± 0.003	20.1 ± 0.5
NaPYG-010	0.620 ± 0.003	0.599 ± 0.004	0.100 ± 0.001	13.7 ± 0.5
NaPYG-020	0.645 ± 0.004	0.581 ± 0.004	0.100 ± 0.001	12.7 ± 0.5
NaPYG-030	0.669 ± 0.003	0.568 ± 0.005	0.060 ± 0.001	15.3 ± 0.5
NaPYG-040	0.686 ± 0.003	0.545 ± 0.002	0.030 ± 0.001	15.6 ± 0.5
NaPYG-050	0.672 ± 0.006	0.520 ± 0.002	0.030 ± 0.001	15.0 ± 0.5
NaPYG-060	0.772 ± 0.005	0.540 ± 0.005	0.020 ± 0.001	4.9 ± 0.5

FIGURES

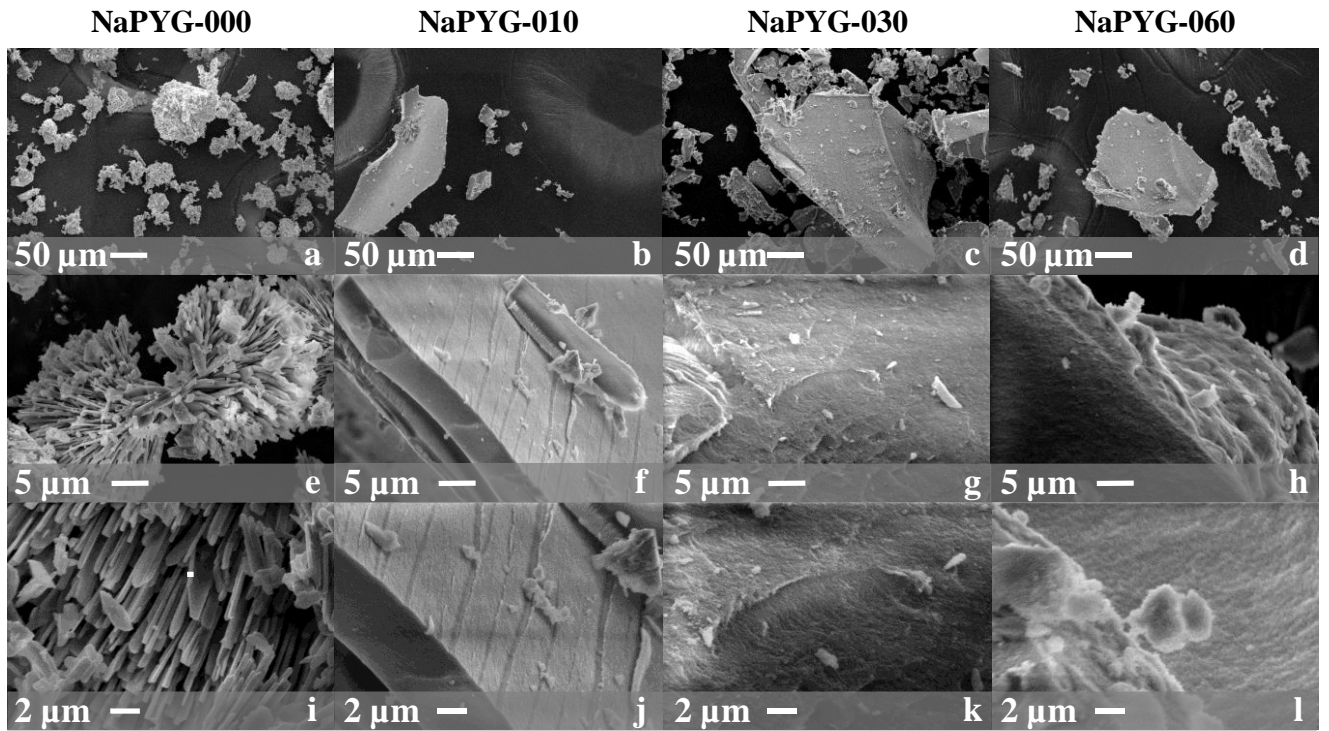


Figure 1: SEM micrographs of synthesized NaPYG materials at different magnifications: NaPYG-000 (a, e, i), NaPYG-010 (b, f, j), NaPYG-030 (c, g, k) and NaPYG-060 (d, h, l).

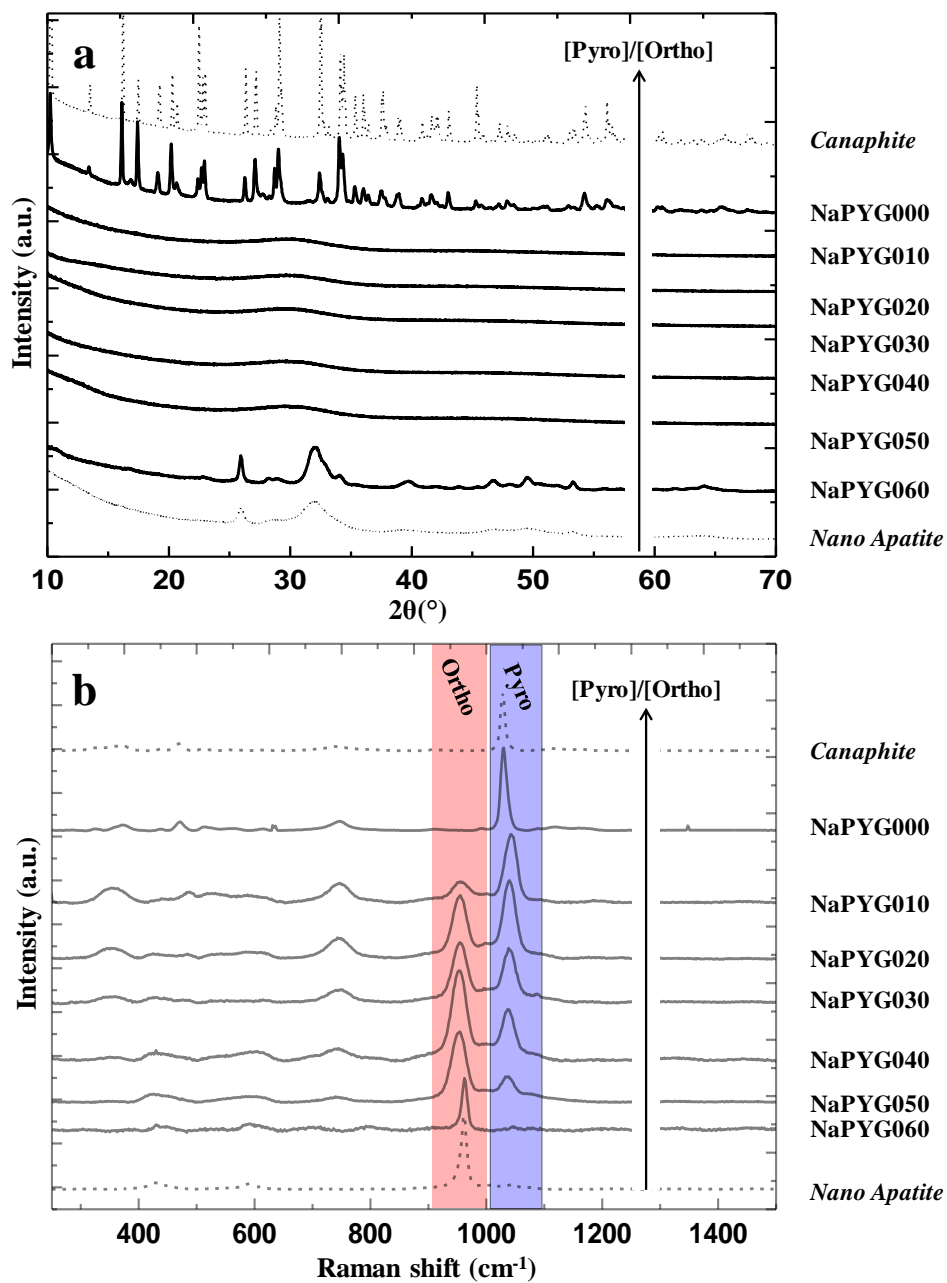


Figure 2: (a) XRD patterns and (b) Raman spectra of NaPYG materials prepared with different ortho/pyrophosphate molar ratios: from NaPYG-000 (top) to NaPYG-060 (bottom). Results for the synthesized canaphite and nanocrystalline apatite reference samples are also presented for comparison. (see supporting information).

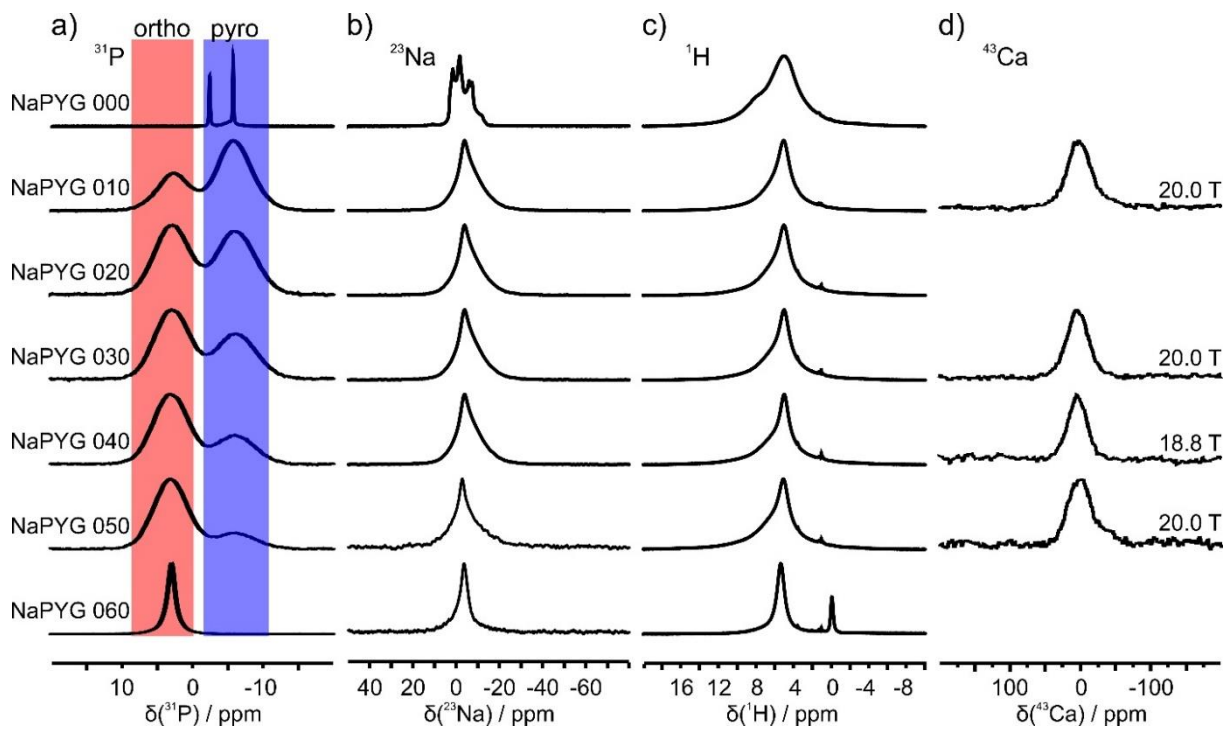


Figure 3. a) ^{31}P single pulse MAS NMR spectra recorded at 14.1 T, using $\nu_r = 14$ kHz. b) ^{23}Na single pulse MAS NMR spectra recorded at 14.1 T using $\nu_r = 20$ kHz. c) ^1H single pulse MAS NMR spectra recorded at 14.1 T using $\nu_r = 40$ kHz. d) ^{43}Ca multi-DFS MAS NMR spectra recorded at 18.8 or 20.0 T using $\nu_r = 4$ -6 kHz. Full details on the acquisition conditions are provided in Supporting Information (SI-2).

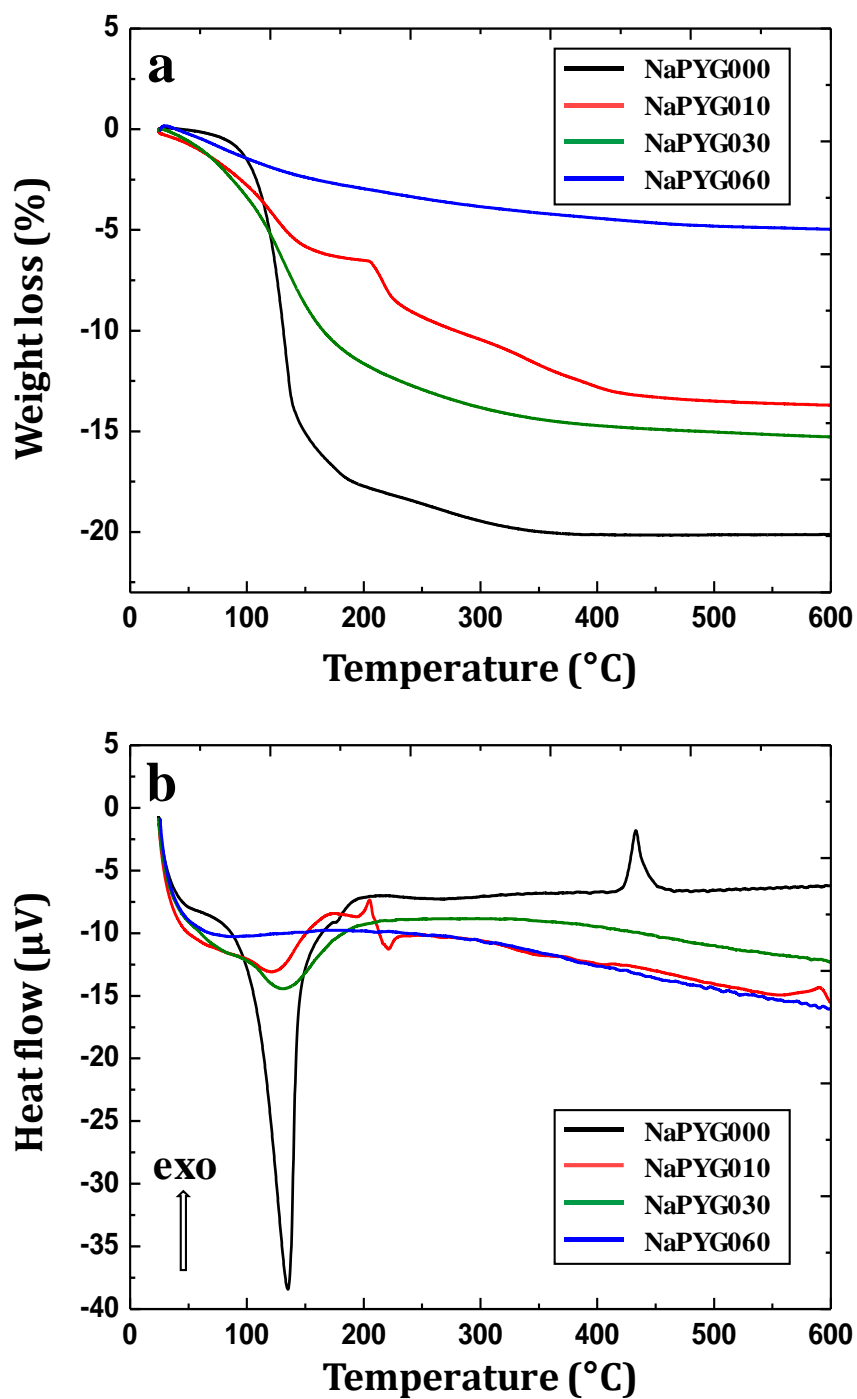


Figure 4. (a) TGA and (b) DTA curves for NaPYG-000, NaPYG-010, NaPYG-030, NaPYG-060 materials. An expansion of the DTA curves is given in Figure S6-c.

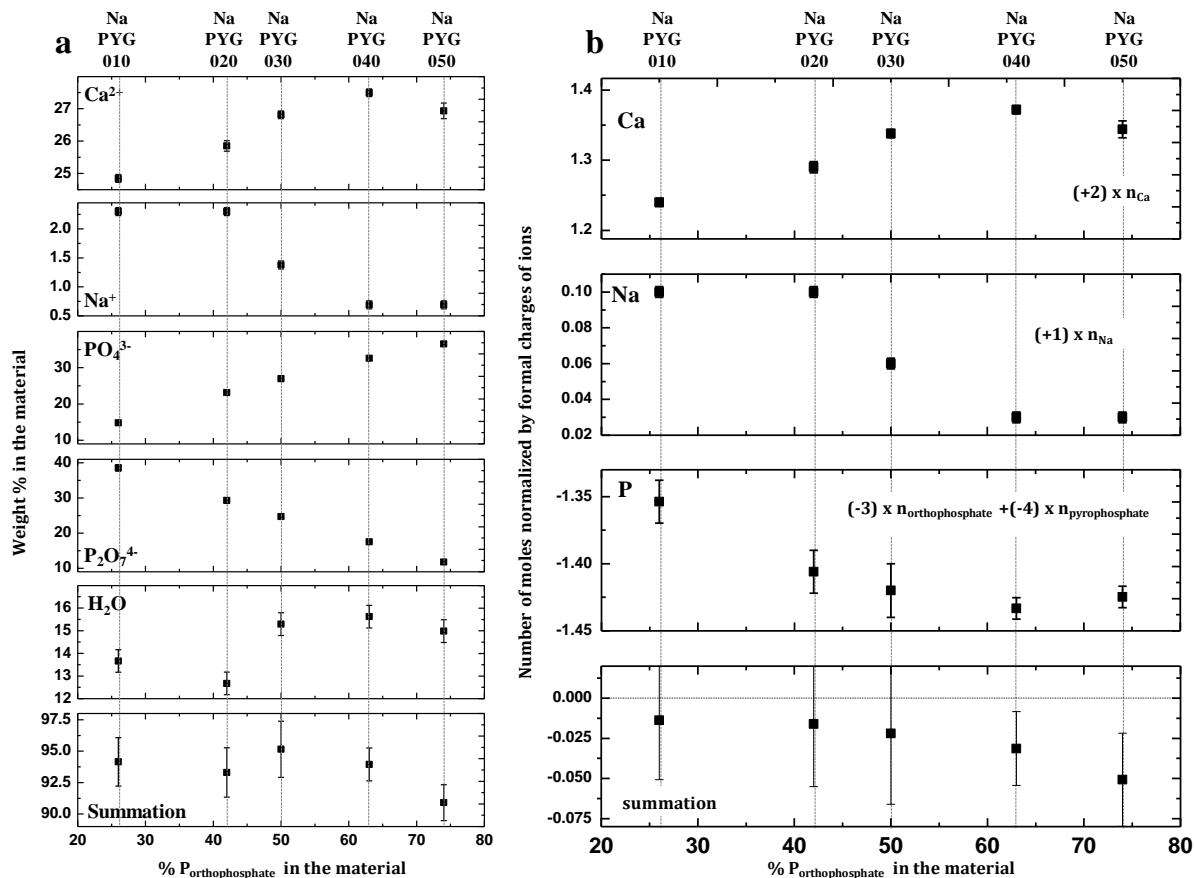


Figure 5. (a) Evolution of weight percentages of Ca^{2+} , Na^+ , PO_4^{3-} , $\text{P}_2\text{O}_7^{4-}$, H_2O , and summation of all these ions and (b) Evolution of charges (number of moles of each ionic entity for 100 g of material normalized by its respective charge) for calcium, sodium, total phosphate and summation for each amorphous NaPYG material (x axis is the percentage of $\text{P}_{\text{orthophosphate}}$ with respect to the total phosphorus content).

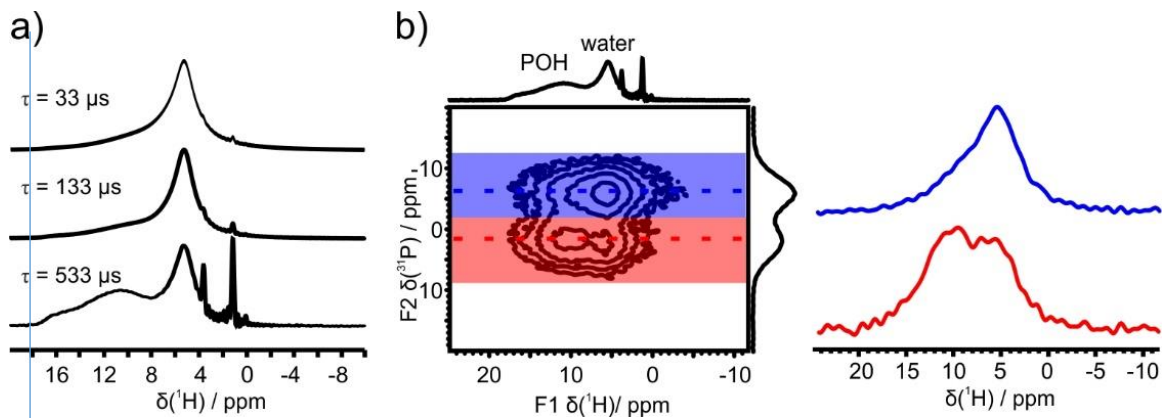


Figure 6. a) ^1H Hahn echo MAS NMR spectra of NaPYG-010 material recorded at 14.1 T, spinning at 22 kHz, using different echo delays ($\tau = 33, 133$ and $533 \mu\text{s}$), showing the presence of protonated phosphate resonances at higher chemical shifts (> 8 ppm); b) $^1\text{H} \rightarrow ^{31}\text{P}$ HETCOR NMR spectrum of NaPYG-010 recorded at 14.1 T, spinning at 22 kHz and using a short contact time (0.1 ms). The ^1H Hahn echo spectrum recorded with $\tau = 533 \mu\text{s}$ is shown on the ^1H projection of the HETCOR. The ^1H NMR spectra in blue and red correspond to the ^1H signals of the HETCOR which correlate with the pyro- and ortho-phosphate species, respectively.

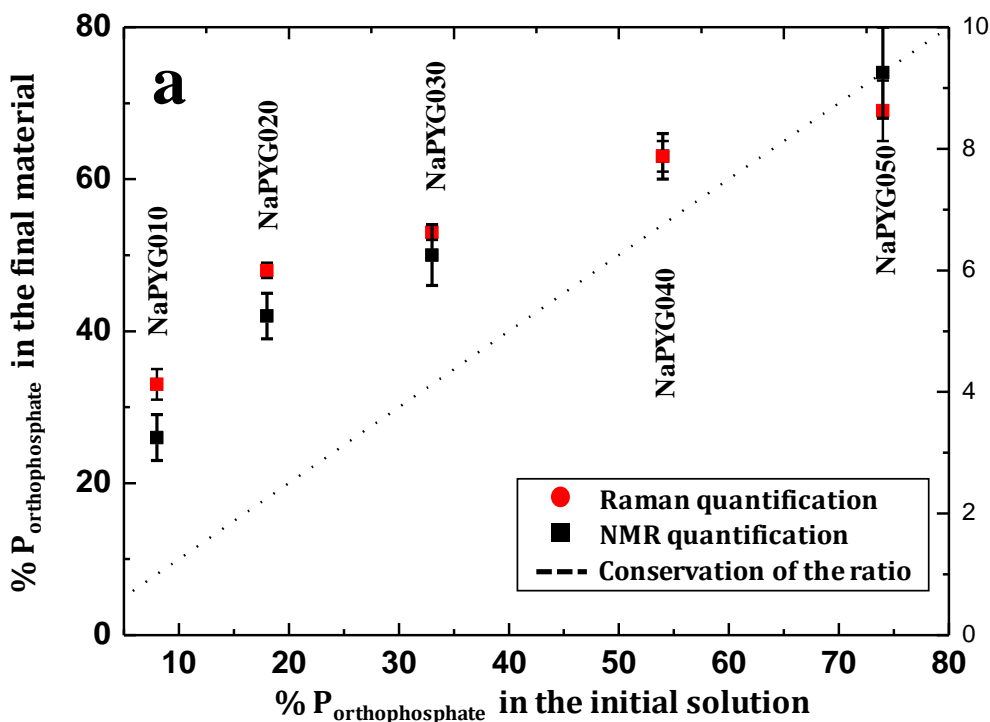


Figure 7. Molar percentage of phosphorus atoms involved in orthophosphate ions (compared to pyrophosphate) in materials (as determined by solid state NMR and Raman spectroscopy) as a function of the molar percentage of orthophosphate ions in the initial precursor solution.

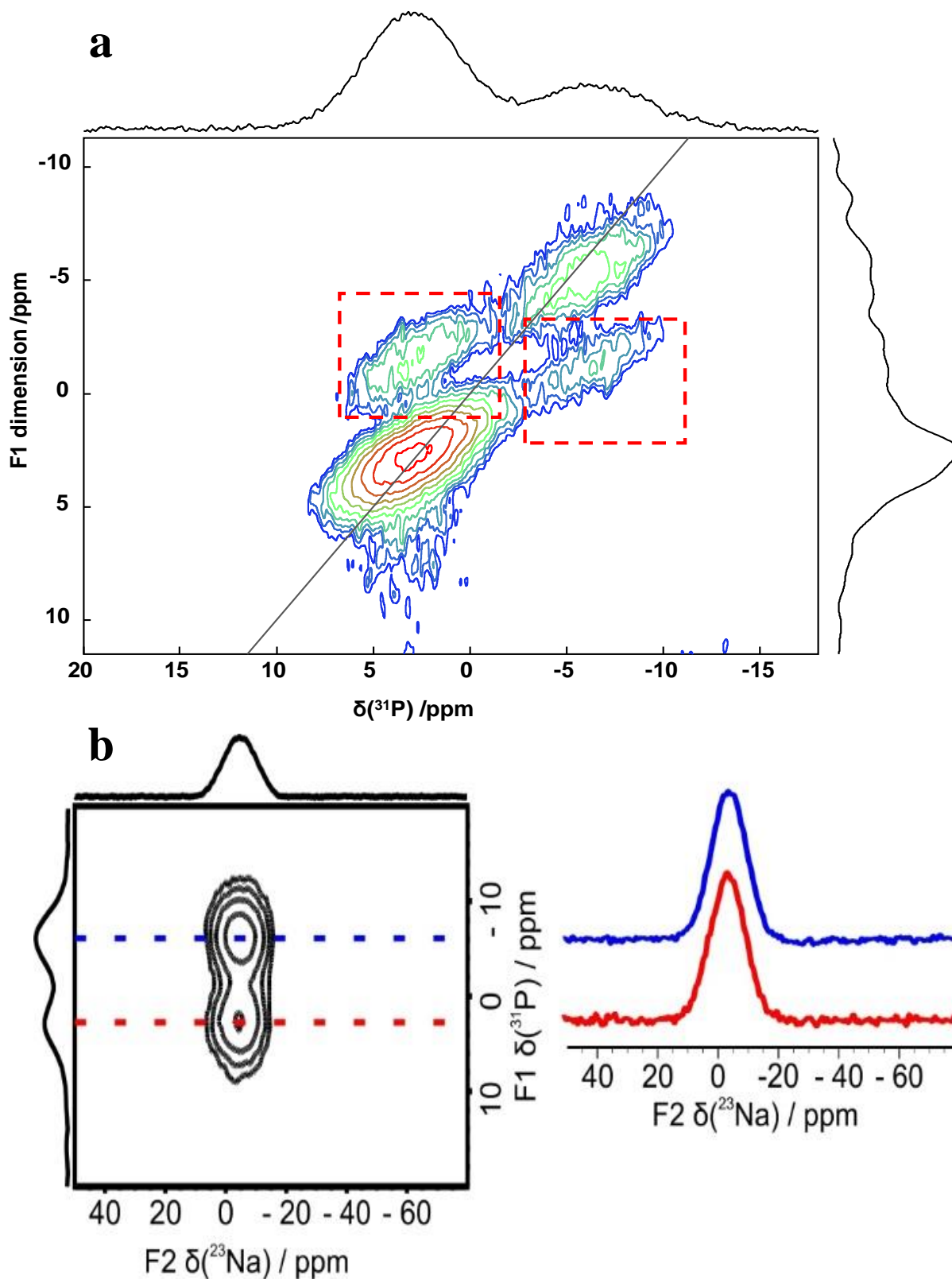


Figure 8. (a) ^{31}P SQ-DQ spectrum of NaPYG030 acquired at 16.4 T, spinning at 14 kHz. The dashed red boxes show the cross-peaks between ortho and pyrophosphate units, (b) $^{23}\text{Na}^{31}\text{P}$ D-HMQC spectrum of NaPYG010 material, acquired at 18.8 T using 20 kHz spinning speed (the ^{23}Na NMR spectra in blue and red correspond to correlations with pyro- and orthophosphate ions, respectively).

References

- [1] A. Hoppe, NS. Gldal, AR. Boccaccini, A review of the biological response to ionic dissolution products from bioactive glasses and glass-ceramics. *Biomater.*, 32 (2011) 2757-2774
- [2] L. L. Hench, The story of Bioglass. *J. Mater. Sci. Mater. Med.* 17 (2006) 967–78.
- [3] J.R. Jones, Review of bioactive glass: from Hench to hybrids. *Acta Biomater.* 9, (2013) 4457-86.
- [4] R. K. Brow. Review: the structure of simple phosphate glasses. *J. Non. Cryst. Solids* (2000) 263-264.
- [5] J.C. Knowles, Phosphate based glasses for biomedical applications. *J. Mater. Chem.* 13, (2003) 2395.
- [6] I. Ahmed, C.A. Collins, M.P. Lewis, I. Olsen, J.C. Knowles, Processing , characterisation and biocompatibility of iron-phosphate glass fibres for tissue engineering. 25, (2004) 3223-3232.
- [7] T. Kasuga, Y. Hosoi, M. Nogamie, Apatite Formation on Calcium Phosphate Invert Glasses in Simulated Body Fluid. 52, (2001) 450-452.
- [8] D.S. Brauer, N. Karpukhina, R.V. Law, R.G. Hill, Effect of TiO₂ addition on structure , solubility and crystallisation of phosphate invert glasses for biomedical applications. *J. Non. Cryst. Solids* 356, (2010) 2626-2633.
- [9] N. Sharmin, C.D. Rudd, A.J. Parsons, I. Ahmed, Structure, viscosity and fibre drawing properties of phosphate-based glasses: effect of boron and iron oxide addition. *J. Mater. Sci.* 51, (2016) 7523-7535.
- [10] C. Combes, C. Rey, Amorphous calcium phosphates: Synthesis, properties and uses in biomaterials. *Acta Biomater.* 6, (2010) 3362-3378.
- [11] D.M. Pickup, R.J. Newport R.J., Barney E.R., Kim J.Y., Valappil S.P. Knowles J.C. Characterisation of phosphate coacervates for potential biomedical applications. *Journal of biomaterials applications* 28, (2014) 226-1234.
- [12] F. Gomez, P. Vas, G. Willot. Influence of pH on the Formation of Polyphosphate Coacervates. *Phosphorus Res. Bull.* 11, (2015) 53-60.
- [13] R.M. Pilliar, R.A. Kandel, M.D. Grynbas, Y. Hu, Porous calcium polyphosphate as load-bearing bone substitutes: In vivo study, *J. Biomed. Mater. Res. - Part B Appl. Biomater.* 101 B (2013) 1–8.
- [14] A. Momeni, M.J. Filiaggi, Comprehensive study of the chelation and coacervation of alkaline earth metals in the presence of sodium polyphosphate solution. *Langmuir* 30, (2014) 5256-5266.
- [15] C. Slater, D. Laurencin, V. Burnell, M.E. Smith, L.M. Grover, J.A. Hriljac A.J. Wright Enhanced stability and local structure in biologically relevant amorphous materials containing pyrophosphate. *J. Mater. Chem.* 21, (2011) 18783-18791.
- [16] P. Gras, C. Rey, O. Marsan, S. Sarda, C. Combes, Synthesis and characterisation of hydrated calcium pyrophosphate phases of biological interest, *Eur. J. Inorg. Chem.* (2013) 5886–5895.
- [17] J. Souli, P. Gras, O. Marsan, D. Laurencin, C. Rey, C. Combes, Development of a new family of monolithic calcium (pyro)phosphate glasses by soft chemistry, *Acta Biomater.* 41 (2016) 320–327.

- [18] C. Rey, C. Combes, C. Drouet, H. Sfihi, A. Barroug, Physico-chemical properties of nanocrystalline apatites: Implications for biominerals and biomaterials, *Mater. Sci. Eng. C*. 27 (2007) 198–205.
- [19] F.J. Gennari, Disorders of potassium homeostasis. Hypokalemia and hyperkalemia. *Crit. Care Clin.* 18 (2002) 273–88.
- [20] L.M. Grover, A.J. Wright, U. Gbureck, A. Bolarinwa, J. Song, Y. Liu, D.F. Farrar, G. Howling, J. Rose, J.E. Barralet, The effect of amorphous pyrophosphate on calcium phosphate cement resorption and bone generation, *Biomaterials*. 34 (2013) 6631–6637.
- [21] S.M. Naga, M. Awaad, H.F. El-Maghraby, A. El-Kady, A. M. Biological performance of calcium pyrophosphate-coated porous alumina scaffolds. *Int. J. Appl. Ceram. Technol.* 11 (2014) 111.
- [22] S. Koo, B. König, S. Allegrini, M. Yoshimoto, M.J. Carbonari, F.F. Mitri-Luiz, Titanium implant osseointegration with calcium pyrophosphate in rabbits, *J. Biomed. Mater. Res. - Part B Appl. Biomater.* 76 (2006) 373–380. doi:10.1002/jbm.b.30383. Koo, S. König, S. Allegrini, M.
- [23] J.H. Lee, B.S. Chang, U.O. Jeung, K.W. Park, M.S. Kim, C.K. Lee, The first clinical trial of beta-calcium pyrophosphate as a novel bone graft extender in instrumented posterolateral Lumbar fusion, *Clin. Orthop. Surg.* 3 (2011) 238–244.
- [24] H. Flodgaard, P. Fleron, Thermodynamic parameters for the hydrolysis of inorganic pyrophosphate at pH 7.4 as a function of $[Mg^{2+}]$, $[K^+]$, and ionic strength determined from equilibrium studies of the reaction, *J. Biol. Chem.* 249 (1974) 3465–3474.
- [25] WN. Addison, F. Azari, ES. Sørensen, MT. Kaartinen, MD. McKnee Pyrophosphate inhibits mineralization of osteoblast cultures by binding to mineral, up-regulating osteopontin, and inhibiting alkaline phosphatase activity., *J. Biol. Chem.*. 282 (2007) 15872-15883.
- [26] JK. Heinonen. *Biological Role of Inorganic Pyrophosphate*, (2001),25, Springer
- [27] N. Vandecandelaère, E. Champion, F. Rossignol, A. Navrotsky, D. Grossin, M. Aufray, S. Rollin-Martinet, C. Drouet, C. Rey, Nanocrystalline apatites: The fundamental role of water, *Am. Mineral.* 103 (2018) 550–564.
- [28] P. Cheng, K.P.H. Pritzker, S.C. Nyburg, Calcium Disodium Pyrophosphate Tetrahydrate, *Acta Crystallogr. B*36 (1980) 921–924.
- [29] F. Fayon, G. Le Saout, L. Emsley, D. Massiot, Through-bond phosphorus-phosphorus connectivities in crystalline and disordered phosphates by solid-state NMR, *Chem. Commun.* 2 (2002) 1702–1703.
- [30] M. Hohwy, C.M. Rienstra, C.P. Jaroniec, R.G. Griffin, Fivefold symmetric homonuclear dipolar recoupling in rotating solids: Application to double quantum spectroscopy, *J. Chem. Phys.* 110 (1999) 7983–7992.
- [31] O. Lafon, Q. Wang, B. Hu, F. Vasconcelos, J. Trébosc, S. Cristol, F. Deng, J.P. Amoureux, Indirect detection via spin-1/2 nuclei in solid state NMR spectroscopy: Application to the observation of proximities between protons and quadrupolar nuclei, *J. Phys. Chem. A*. 113 (2009) 12864–12878.
- [32] F.A. Perras, J. Viger-Gravel, K.M.N. Burgess, D.L. Bryce, Signal enhancement in solid-state NMR of quadrupolar nuclei, *Solid State Nucl. Magn. Reson.* 51–52 (2013) 1–15.
- [33] Z. Gan, I. Hung, X. Wang, J. Paulino, G. Wu, I.M. Litvak, P.L. Gor'kov, W.W. Brey, P. Lendi, J.L. Schiano, M.D. Bird, I.R. Dixon, J. Toth, G.S. Boebinger, T.A. Cross, NMR spectroscopy up to 35.2 T using a series-connected hybrid magnet, *J. Magn. Reson.* 284 (2017) 125–136.
- [34] C. Bonhomme, X. Wang, I. Hung, Z. Gan, C. Gervais, C. Sassoie, J. Rimsza, J. Du, M.E. Smith, J. V. Hanna, S. Sarda, P. Gras, C. Combes, D. Laurencin, Pushing the limits of sensitivity and

resolution for natural abundance ^{43}Ca NMR using ultra-high magnetic field (35.2 T), *Chem. Commun.* 54 (2018) 9591–9594.

- [35] L.L.H. Pilar Sepulveda, Julian R. Jones, Characterization of Melt-Derived 45S5 and sol-gel-derived 58S Bioactive Glasses, *J. Biomed. Mater. Res.* (2001) 564–569.
- [36] C. Rouse, D. Peacor, R. Freed, Pyrophosphate groups in the structure of canaphite : The first phosphate as a mineral occurrence of a condensed phosphate as a mineral, 7 (1988) 161–171.
- [37] [1] H.E. Mason, A. Kozłowski, B.L. Phillips, Solid-state NMR study of the role of H and Na in AB-type carbonate hydroxylapatite-Supporting Information 1, (2008) 1–6.
- [38] P. Gras, A. Baker, C. Combes, C. Rey, S. Sarda, A.J. Wright, M.E. Smith, J. V. Hanna, C. Gervais, D. Laurencin, C. Bonhomme, From crystalline to amorphous calcium pyrophosphates: A solid state Nuclear Magnetic Resonance perspective, *Acta Biomater.* 31 (2016) 348–357.
- [39] E. Gambuzzi, A. Pedone, M.C. Menziani, F. Angeli, P. Florian, T. Charpentier, Calcium environment in silicate and aluminosilicate glasses probed by ^{43}Ca MQMAS NMR experiments and MD-GIPAW calculations, *Solid State Nucl. Magn. Reson.* 68 (2015) 31–36.
- [40] S. Rollin-Martinet, A. Navrotsky, E. Champion, D. Grossin, C. Drouet, Thermodynamic basis for evolution of apatite in calcified tissues., *Am. Mineral.* 98 (2013) 2045.
- [41] J.T.B. Ratnayake, M. Mucalo, G.J. Dias, Substituted hydroxyapatites for bone regeneration: A review of current trends, *J. Biomed. Mater. Res. - Part B Appl. Biomater.* 105 (2017) 1285–1299.
- [42] J. Soulié, J. Lao, E. Jallot, J.M. Nedelec, Influence of mesostructuration on the reactivity of bioactive glasses in biological medium: a PIXE-RBS study, *J. Mater. Chem.* 22 (2012) 20680.
- [43] Brinker, C. & Scherer, G. Sol \rightarrow gel \rightarrow glass: I. Gelation and gel structure. 70, (1985) 301–322.
- [44] D. Grossin, S. Rollin-Martinet, C. Estournès, F. Rossignol, E. Champion, C. Combes, C. Rey, C. Geoffroy, C. Drouet, Biomimetic apatite sintered at very low temperature by spark plasma sintering: Physico-chemistry and microstructure aspects, *Acta Biomater.* 6 (2010) 577–585.
- [45] [F. Pourpoint, C. Gervais, L. Bonhomme-Coury, T. Azaïs, C. Coelho, F. Mauri, B. Alonso, F. Babonneau, C. Bonhomme, Calcium phosphates and hydroxyapatite: Solid-state NMR experiments and first-principles calculations, *Appl. Magn. Reson.* 32 (2007) 435–457.
- [45] D.S. Brauer, C. Rüssel, J. Kraft, Solubility of glasses in the system $\text{P}_2\text{O}_5\text{-CaO-MgO-Na}_2\text{O-TiO}_2$: Experimental and modeling using artificial neural networks, *J. Non. Cryst. Solids.* 353 (2007) 263–270.
- [46] D.S. Brauer, R.M. Wilson, T. Kasuga, Multicomponent phosphate invert glasses with improved processing, *J. Non. Cryst. Solids.* 358 (2012) 1720–1723.
- [47] F. Herbert, B. Sylvia, Mechanism of calcification: inhibitory role of pyrophosphate, *Nature.* (1962) 911.
- [48] N. Eidelman, W.E. Brown, The effect of pyrophosphate concentrations on calcium phosphate growth on well-crystallized octacalcium phosphate and hydroxyapatite seed crystals, 108 (1990) 385–393.
- [49] C. Thouverey, G. Bechkoff, S. Pikula, R. Buchet, Inorganic pyrophosphate as a regulator of hydroxyapatite or calcium pyrophosphate dihydrate mineral deposition by matrix vesicles, *Osteoarthr. Cartil.* 17 (2009) 64–72.
- [50] F. Betts, A.S. Posner, An X-ray radial distribution study of amorphous calcium phosphate, *Mater. Res. Bull.* 9 (1974) 353–360.

- [51] G. Treboux, P. Layrolle, N. Kanzaki, K. Onuma, A. Ito, Existence of posner's cluster in vacuum, *J. Phys. Chem. A.* 104 (2000) 5111–5114.
- [52] M. Andersson, Transformation of amorphous calcium phosphate to bone-like apatite, *Nat. Commun.* (2018).
- [53] Gras, P. Etude Physico-Chimique Et Structurale De Pyrophosphates De Calcium Hydrates: Application Aux Micro-Calcifications Associees a L'Arthrose. PhD. Univ. Toulouse (2014) 208.
- [54] N.H. De Leeuw, D. Di, N.H. De Leeuw, Detection of Posner's clusters during calcium phosphate nucleation: a molecular dynamics study, *J. Mater. Chem. B.* 5 (2017) 7274–7284.
- [55] X. Yang, M. Wang, Y. Yang, B. Cui, Z. Xu, X. Yang, Physical origin underlying the prenucleation-cluster-mediated nonclassical nucleation pathways for calcium phosphate, *Phys. Chem. Chem. Phys.* 9 (2019).

SUPPORTING INFORMATION

A novel soft-chemistry approach to the synthesis of amorphous calcium ortho/pyrophosphate biomaterials of tunable composition

Laëtitia Mayen^{a,‡}, Nicolai D. Jensen^{b,c,‡}, Danielle Laurencin^b, Olivier Marsan^a, Christian Bonhomme^c, Christel Gervais^c, Mark E. Smith^d, Cristina Coelho^c, Guillaume Laurent^c, Julien Trebosc^c, Zhehong Gan^f, Kuizhi Chen^f, Christian Rey^a, Christèle Combes^a, Jérémy Soulié^{a*}

^aCIRIMAT, Université de Toulouse, CNRS, INPT-ENSIACET, Toulouse, France

^bICGM, CNRS-UM-ENSCM, Université de Montpellier, Montpellier, France

^cSorbonne Université, CNRS, LCMCP, Paris, France

^dDepartment of Chemistry, Lancaster University, Lancaster, UK

^eUniversité de Lille, UMR 8181, UCCS: Unit of Catalysis and Chemistry of Solids, Lille, France

^fNational High Magnetic Field Laboratory, Tallahassee, FL, USA

[‡]These authors contributed equally to the work.

*Corresponding author.

E-mail address: jeremy.soulie@toulouse-inp.fr

SI-1: Synthesis of α -canaphite

SI-2: Full experimental details of the solid state NMR experiments.

SI-3: Methodology for the determination of the orthophosphate and pyrophosphate proportions from Raman spectra

SI-4: ³¹P CP-INADEQUATE and CPMAS solid state NMR spectra

SI-5: ²³Na solid state NMR data, including spectral deconvolutions

SI-6: ⁴³Ca solid state NMR data of NaPYG-050, recorded at both 20.0 T and 35.2 T.

SI-7: TGA and DTA of NaPYG-020, NaPYG-030, NaPYG-040, NaPYG-050 samples.

SI-8: Mass percentages of Ca²⁺, Na⁺, PO₄³⁻, P₂O₇⁴⁻ and H₂O in NaPYG materials.

SI-9: TEM picture of NaPYG030 sample.

SI-10: Comparison of ³¹P and ²³Na NMR spectra of materials from different synthetic batches of NaPYG-010.

SI-11: ¹H Hahn echo spectra of NaPYG materials, and ¹H→³¹P HETCOR study of NaPYG-010.

SI-12: XRD diagrams and Raman spectra of NaPYG materials obtained without the washing step.

SI-1: Synthesis of α -canaphite

Calcium and phosphate reagent solutions were prepared separately by dissolving $\text{CaCl}_2 \cdot 2\text{H}_2\text{O}$ in 40 mL of deionized water (solution A) and pyrophosphate ($\text{Na}_4\text{P}_2\text{O}_7$) precursor in 400 mL of deionized water (Solution B). Solution B was prepared with the same precursor as described in the NaPYG synthesis protocol. Solution A was then added to solution B using a peristaltic pump at a constant volumetric flowrate ($8 \text{ mL} \cdot \text{min}^{-1}$). The mixture was first transparent, and after the addition completed, the solution was left to mature under magnetic stirring for 20 hours, during which the suspension becomes white. The solution was filtrated on Buchner funnel, using microporous filters (Sartorius 391 for particles size of $2/3 \mu\text{m}$). The resulting powder was washed three times with 200 mL of deionized water. Finally, the final powder was poured into a glass crystallizer and dried at 37°C for one night. This powder was identified as pure α -canaphite by XRD, Raman and ^{31}P solid state NMR.

SI-2: Complete experimental details regarding the solid state NMR experiments.

^1H , ^{31}P , $^1\text{H} \rightarrow ^{31}\text{P}$ CP, ^{31}P CP-INADEQUATE (14.1 T)

^1H single pulse, ^{31}P single pulse and ^{31}P CP-INADEQUATE spectra were recorded on a VNMRS-600 MHz spectrometer equipped with a 3.2 mm triple resonance MAS probe operating in dual resonance mode, and tuned to ^1H ($\nu_0 = 599.82 \text{ MHz}$) and ^{31}P ($\nu_0 = 242.81 \text{ MHz}$). The ^{31}P single pulse experiments were recorded at $\nu_r = 14 \text{ kHz}$, using a $2.5 \mu\text{s}$ 90° pulse, and spinal-64 ^1H decoupling (RF = 100 kHz) during acquisition. A recycle delay of 400 s was used for all samples (except NaPYG-000, with D1 = 800 s), and 4 scans were acquired. The ^{31}P CP-INADEQUATE spectra were recorded using 16 to 20 kHz spinning speeds. A ^{31}P RF power of 83 kHz or 100 kHz was used for the 90° and 180° pulses, depending on the sample, and the evolution delay was set to 4 ms. Spinal-64 ^1H decoupling (RF = 100 kHz) was applied during acquisition. Experiments were performed using 10 pre-saturation pulses on the ^{31}P , 80 to 400 s recycle delays, and collecting 16 to 64 scans, depending on the sample. $^1\text{H} \rightarrow ^{31}\text{P}$ CP MAS was recorded using at $\nu_r = 14 \text{ kHz}$, using a $2.5 \mu\text{s}$ 90° pulse and a contact time of 300 μs , 2 ms and 8 ms. A recycle delay of 8 s (16 s for NaPYG 000) and 20 scans were collected, spinal-64 decoupling (RF = 100 kHz) was applied during acquisition. The ^{31}P CP-INADEQUATE of NaPYG-010, NaPYG-030 and NaPYG-050 were performed with the temperature control unit set to 0°C , while all other experiments were performed without temperature control. Chemical shifts were referenced relative to hydroxyapatite to $\delta_{\text{iso}}(^1\text{H}) = 0 \text{ ppm}$ (on hydroxyl group) for ^1H and $\delta_{\text{iso}}(^{31}\text{P}) = 2.8 \text{ ppm}$ for ^{31}P .

^1H single pulse and ^1H Hahn echo (14.1 T)

^1H single pulse and ^1H Hahn echo spectra were recorded on a VNMRS-600 MHz spectrometer equipped with a Varian 1.2 mm triple resonance MAS probe tuned to ^1H ($\nu_0 = 599.82 \text{ MHz}$), and using a 40 kHz spinning speed. The ^1H single pulse experiments were performed using a $2.5 \mu\text{s}$ 90° pulse (RF = 100 kHz). The ^1H Hahn echo experiment were recorded using $2.5 \mu\text{s}$ and $5.0 \mu\text{s}$ 90° and 180° pulses, and rotor-synchronised echo delays $\tau = 25 \mu\text{s}$, $250 \mu\text{s}$ and $500 \mu\text{s}$. A total of 32 scans were acquired, with a recycle delay of 8 s (16 s for NaPYG-000). Chemical shifts were referenced relative to adamantane ($\delta_{\text{iso}}(^1\text{H}) = 1.8 \text{ ppm}$ for ^1H).

^{23}Na single pulse (9.4 and 14.1 T)

The ^{23}Na single pulse experiments were performed on a VNMRS-600 MHz spectrometer (14.1 T) using a Varian 3.2 mm triple resonance MAS probe tuned to ^1H ($\nu_0 = 599.82 \text{ MHz}$) and ^{23}Na ($\nu_0 = 158.66 \text{ MHz}$), and spinning at $\nu_r = 20 \text{ kHz}$. The ^{23}Na single pulse experiments were performed using $0.5 \mu\text{s}$ 30° or $1.5 \mu\text{s}$ 90° solid pulses, and applying spinal-64 ^1H decoupling (RF = 100 kHz) during acquisition. Comparison of ^{23}Na lineshapes obtained using 0.5 or $1.5 \mu\text{s}$ pulses showed no significant variation. Recycle delays of 0.2 to 2 s were used, and 200 to 12000 scans were collected, depending on the sample. Complementary ^{23}Na single pulse experiments were performed on a VNMRS-400 MHz spectrometer (9.4 T) using a Varian 3.2 mm triple resonance MAS probe, tuned to ^1H ($\nu_0 = 399.93 \text{ MHz}$) and ^{23}Na ($\nu_0 = 105.79 \text{ MHz}$), and spinning at $\nu_r = 20 \text{ kHz}$. The ^{23}Na single pulse experiments were performed using a $0.5 \mu\text{s}$ 30° solid pulse (RF $\approx 83 \text{ kHz}$), and applying spinal-64 ^1H decoupling (RF = 100 kHz) during

acquisition. Recycle delays of 0.2 to 0.5 s were used, and 12000 to 20000 scans were collected, depending on the sample. Chemical shifts were referenced relative to a 1 M NaCl solution (at 0 ppm). The ^{23}Na single pulse experiments using a 0.5 μs pulse were collected with the temperature control set to 0 °C, while the ^{23}Na single pulse experiment collected using a 2.5 μs pulse were collected without temperature control. No significant influence was observed on the spectra in presence of temperature regulation.

^1H Hahn echo and $^1\text{H}\{^{31}\text{P}\}$ HETCOR (14.1 T)

^1H Hahn echo and $^1\text{H}\{^{31}\text{P}\}$ HETCOR NMR spectra were acquired using a VNMRS-600 MHz spectrometer equipped with a Varian 1.6 mm triple resonance MAS probe operating in dual resonance mode, and tuned to ^1H ($\nu_0 = 599.82$ MHz) and ^{31}P ($\nu_0 = 242.81$ MHz). The ^1H Hahn echo spectra were recorded spinning at 30 kHz, using a 2.5 μs (90°) and 5.0 μs (180°) pulses (RF = 100 kHz), and echo delays corresponding to 1, 3, 4, 12, 13, 16 rotor periods. A total of 32 scans was acquired with a recycle delay of 4 s. The $^1\text{H}\{^{31}\text{P}\}$ CP-HETCOR were acquired at $\nu_r = 22$ kHz, using a 3 μs 90° pulse and contact times of 0.1, 0.3 and 5.0 ms. Spinal-64 ^1H decoupling (RF = 100 kHz) was applied during acquisition. Chemical shifts were referenced relative to hydroxyapatite to $\delta_{\text{iso}}(^1\text{H}) = 0$ ppm (on hydroxyl group) for ^1H and $\delta_{\text{iso}}(^{31}\text{P}) = 2.8$ ppm for ^{31}P . The experiments were performed with the temperature control unit set to -40 °C.

^{31}P CP SQ-DQ (16.4 T)

The ^{31}P CP SQ-DQ experiment was performed on a 700 MHz (16.4 T) Bruker Avance III spectrometer, using a 4.0 mm double resonance MAS probe, and tuned to ^1H ($\nu_0 = 700.14$ MHz) and ^{31}P ($\nu_0 = 283.42$ MHz), spinning at $\nu_r = 14$ kHz. The recoupling was performed using the SPC5 scheme,¹ with 571 μs recoupling periods ($L_0 = 20$). A contact time of 1 ms was used for CP transfer, and spinal-64 ^1H decoupling was applied during evolution and acquisition periods. The recycle delay was 3s, and 384 scans were acquired for each of the increments in the 2D. The experiments were performed without temperature regulation. Chemical shifts were referenced relative to phenylphosphinic acid ($\delta_{\text{iso}}(^{31}\text{P}) = 19.7$ ppm).²

$^{23}\text{Na}\{^{31}\text{P}\}$ D-HMQC (18.8 T)

The DFS enhanced $^{23}\text{Na}\{^{31}\text{P}\}$ D-HMQC spectra were recorded on a 800 MHz Bruker Avance NEO 4 (18.8 T) instrument equipped with a 3.2 mm HXY probe and spinning at $\nu_r = 20$ kHz. The DFS- $^{23}\text{Na}\{^{31}\text{P}\}$ D-HMQC spectra were acquired with direct detection of the quadrupole nucleus using the previously published sequence,³ using a 1600 μs SFAM2 recoupling pulse, using the $q = 1$ condition. The following experimental parameters were used: 10 μs 90° ^{23}Na solid pulse, 4 μs ^{31}P 90° pulse, ^1H decoupling (63 kHz RF) during recoupling and acquisition periods. A recycle delay of 0.4 s was used, and 1536 scans were acquired for each of the 30 increments. The chemical shifts were referenced to $\delta_{\text{iso}}(^{23}\text{Na}) = 0$ ppm on a 1M NaCl solution, and to $\delta_{\text{iso}}(^{31}\text{P}) = 0$ ppm on orthophosphoric acid. The experiments were performed without temperature control.

Natural abundance ^{43}Ca solid state NMR (18.8, 20.0 and 35.2 T)

^{43}Ca NMR spectra were recorded at three different fields, depending on the sample.

^{43}Ca NMR experiments were performed at 18.8 T on a 800 MHz Bruker Avance NEO 4 spectrometer, equipped with a 4 mm HX Tallahassee MAS probe tuned to ^{43}Ca ($\nu_0 = 53.85$ MHz), and using 6 kHz spinning speed. The spectra were acquired using a multi-QFS pulse with 16 repetitions, using a sweeping from 210 to 190 kHz and 110 to 90 kHz followed by a 8 μs pulse (RF \approx 8 kHz). The recycle delay was set to 0.4 s, 9000 to 63000 scans were recorded, depending on the sample.

^{43}Ca NMR experiments were performed at 20.0 T on a Bruker NEO spectrometer, using a 7 mm X low gamma MAS probe tuned to ^{43}Ca ($\nu_0 = 57.22$ MHz), using a 5 kHz spinning speed. The spectra were

¹ M. Hohwy, C. M. Rienstra, C. P. Jaroniec, R. G. Griffin, *J. Chem. Phys.* **1999**, *110*, 7983.

² C. Gervais, C. Coelho, T. Azais, J. Maquet, G. Laurent, F. Pourpoint, C. Bonhomme, P. Florian, B. Alonso, G. Guerrero, P. H. Mutin, F. Mauri, *J. Magn. Reson.* **2007**, *187*, 131.

³ O. Lafon, Q. Wang, B. Hu, F. Vasconcelos, J. Trébosc, S. Cristol, F. Deng, J. P. Amoureux, *J. Phys. Chem. A*, **2009**, *113*, 12864-12878.

acquired using a multi-DFS enhancement (400 to 50 kHz DFS sweep), followed by a 1.5 μ s pulse (RF \approx 27 kHz). The recycle delay was set to 0.3 s, and a total of 47000 to 70000 scans were collected, depending on the sample.

^{43}Ca NMR experiments were performed at 35.2 T on an SCH magnet in Tallahassee,⁴ equipped with a single channel 3.2 mm MAS probe, tuned to ^{43}Ca ($\nu_0(^{43}\text{Ca}) = 100.96$ MHz) and spinning at 10 kHz. NMR experiments were performed using a Bruker Advance NEO console. A multi-DFS pulse sequence was used, The recycle delay was set to 0.2 s, and \sim 11000 scans were acquired.

All ^{43}Ca NMR spectra were referenced on 1 M CaCl_2 ($\delta_{\text{iso}}(^{43}\text{Ca}) = 0$ ppm), and the powers were calibrated on a saturated CaCl_2 solution. No temperature control was applied during ^{43}Ca measurements.

⁴ Z. Gan, I. Hung, X. L. Wang, J. Paulino, G. Wu, I. M. Litvak, P. L. Gor'kov, W. W. Brey, P. Lendi, J. L. Schiano, M. D. Bird, L. R. Dixon, J. Toth, G. S. Boebinger, T. A. Cross, *J. Magn. Reson.* **2017**, *284*, 125

Table S1. List of NMR parameters used for each sample.

Sample	Sequence	Spin	Field (T)	Rotor Ø (mm)	ν_r (kHz)	D1 (s)	NS	Temp. control	Reference	Figure
NaPYG 000	Single pulse	^1H	14.1	1.2	40	16	32	-	Adamantane	3, S8
	Hahn echo	^1H	14.1	1.2	40	16	32	-	Adamantane	S8
	Single pulse (90°)	^{23}Na	14.1	3.2	20	2	80	-	1 M NaCl	3
	Single pulse	^{31}P	14.1	3.2	14	800	4	-	Apatite	3
	CP (CT = 300 μs)	^{31}P	14.1	3.2	14	16	20	-	Apatite	S1
	CP (CT = 2 ms)	^{31}P	14.1	3.2	14	16	20	-	Apatite	S1
	CP (CT = 8 ms)	^{31}P	14.1	3.2	14	16	20	-	Apatite	S1
NaPYG 010	Single pulse	^1H	14.1	1.2	40	8	32	-	Adamantane	3, S8
	Hahn echo	^1H	14.1	1.2	40	8	32	-	Adamantane	S8
	Single pulse (90°)	^{23}Na	14.1	3.2	20	2	200	-	1 M NaCl	3
	Single pulse (30°)	^{23}Na	14.1	3.2	20	0.3	6k	0°C	1 M NaCl	S2
	Single pulse (30°)	^{23}Na	9.4	3.2	20	0.3	10k	0°C	1 M NaCl	S2
	Single pulse	^{31}P	14.1	3.2	14	400	4	-	Apatite	3
	CP-INADEQUATE	^{31}P	14.1	3.2	18	2	256	0°C	Apatite	S1
	CP (CT = 300 μs)	^{31}P	14.1	3.2	14	8	20	-	Apatite	S1
	CP (CT = 2 ms)	^{31}P	14.1	3.2	14	8	20	-	Apatite	S1
	CP (CT = 8 ms)	^{31}P	14.1	3.2	14	8	20	-	Apatite	S1

	HETCOR (CT = 5 ms)	¹ H ³¹ P	14.1	1.6	22	3	20 ()	-40°C	Apatite	S9
	HETCOR (CT = 0.3 ms)	¹ H ³¹ P	14.1	1.6	22	3	92	-40°C	Apatite	S9
	HETCOR (CT = 0.1 ms)	¹ H ³¹ P	14.1	1.6	22	3	136	-40°C	Apatite	7, S9
	D-HMQC	²³ Na ³¹ P	18.8	3.2	20	0.4	153 2	-	1 M NaCl, phosphori c acid	S11
	Multi- DFS	⁴³ Ca	20	7	5	0.3	47k	-	1 M CaCl ₂	3
NaPYG 020	Single pulse	¹ H	14.1	1.2	40	8	32	-	Adamanta ne	3, S8
	Hahn echo	¹ H	14.1	1.2	40	8	32	-	Adamanta ne	S8
	Single pulse (90°)	²³ Na	14.1	3.2	20	2	200	-	1 M NaCl	3
	Single pulse	³¹ P	14.1	3.2	14	800	4	-	Apatite	3
	CP (CT = 300 μs)	³¹ P	14.1	3.2	14	8	20	-	Apatite	S1
	CP (CT = 2 ms)	³¹ P	14.1	3.2	14	8	20	-	Apatite	S1
	CP (CT = 8 ms)	³¹ P	14.1	3.2	14	8	20	-	Apatite	S1
NaPYG 030	Single pulse	¹ H	14.1	1.2	40	8	32	-	Adamanta ne	3, S8
	Hahn echo	¹ H	14.1	1.2	40	8	32	-	Adamanta ne	S8
	Single pulse (90°)	²³ Na	14.1	3.2	20	2	200	-	1 M NaCl solution	3
	Single pulse (30°)	²³ Na	14.1	3.2	20	0.5	6k	0°C	1 M NaCl solution	S2
	Single pulse (30°)	²³ Na	9.4	3.2	20	0.3	10k	0°C	1 M NaCl solution	S2

	Single pulse	³¹ P	14.1	3.2	14	400	4	-	Apatite	3
	CP-INADEQUATE	³¹ P	14.1	3.2	20	3	768	0°C	Apatite	S1
	CP (CT = 300 μs)	³¹ P	14.1	3.2	14	8	20	-	Apatite	S1
	CP (CT = 2 ms)	³¹ P	14.1	3.2	14	8	20	-	Apatite	S1
	CP (CT = 8 ms)	³¹ P	14.1	3.2	14	8	20	-	Apatite	S1
	CP-SQ-DQ	³¹ P	16.4	4	14	3	384	-	Phenylphosphinic acid	8
	Multi-DFS	⁴³ Ca	20.0	7	5	0.3	70k	-	1 M CaCl ₂	3, S5
NaPYG 040	Single pulse	¹ H	14.1	1.2	40	8	32	-	Adamantane	3, S8
	Hahn echo	¹ H	14.1	1.2	40	8	32	-	Adamantane	S8
	Single pulse (90°)	²³ Na	14.1	3.2	20	2	200	-	1 M NaCl solution	3
	Single pulse	³¹ P	14.1	3.2	14	400	4	-	Apatite	3
	CP (CT = 300 μs)	³¹ P	14.1	3.2	14	8	20	-	Apatite	S1
	CP (CT = 2 ms)	³¹ P	14.1	3.2	14	8	20	-	Apatite	S1
	CP (CT = 8 ms)	³¹ P	14.1	3.2	14	8	20	-	Apatite	S1
	Multi-DFS	⁴³ Ca	18.8	4	6	0.4	60 k	-	1 M CaCl ₂	3
NaPYG 050	Single pulse	¹ H	14.1	1.2	40	8	32	-	Adamantane	3, S8
	Hahn echo	¹ H	14.1	1.2	40	8	32	-	Adamantane	S8
	Single pulse (90°)	²³ Na	14.1	3.2	20	2	200	-	1 M NaCl solution	3
	Single pulse (30°)	²³ Na	14.1	3.2	20	0.2	12k	0°C	1 M NaCl solution	S3

	Single pulse (30°)	²³ Na	9.4	3.2	20	0.2	20k	0°C	1 M NaCl solution	S3
	Single pulse	³¹ P	14.1	3.2	14	400	4	-	Apatite	3
	CP-INADEQUATE	³¹ P	14.1	3.2	18	2	512	0 °C	Apatite	S1
	CP (CT = 300 μs)	³¹ P	14.1	3.2	14	8	20	-	Apatite	S1
	CP (CT = 2 ms)	³¹ P	14.1	3.2	14	8	20	-	Apatite	S1
	CP (CT = 8 ms)	³¹ P	14.1	3.2	14	8	20	-	Apatite	S1
	Multi-DFS	⁴³ Ca	20.0	7	5	0.3	56k	-	1 M CaCl ₂	3, S5
	Multi-DFS	⁴³ Ca	35.2	3.2	10	0.2	10k	-		S5
NaPYG 060	Single pulse	¹ H	14.1	1.2	40	8	32	-	Adamantane	3, S8
	Hahn echo	¹ H	14.1	1.2	40	8	32	-	Adamantane	S8
	Single pulse (90°)	²³ Na	14.1	3.2	20	2	200	-	1 M NaCl solution	3
	Single pulse	³¹ P	14.1	3.2	14	400	4	-	Apatite	3
	CP (CT = 300 μs)	³¹ P	14.1	3.2	14	8	20	-	Apatite	S1
	CP (CT = 2 ms)	³¹ P	14.1	3.2	14	8	20	-	Apatite	S1
	CP (CT = 8 ms)	³¹ P	14.1	3.2	14	8	20	-	Apatite	S1

SI-3: Methodology for the determination of the orthophosphate and pyrophosphate proportions from Raman spectra.

The treatment of the spectra and their decomposition for semi-quantitative analysis of the phosphate species involved in NaPYG materials was carried out using the software Labspec5 (Horiba). For all spectra, a correction of the baseline was applied and the decomposition was carried out over the 850 to 1200 cm^{-1} range considering nine bands have been used (**Table S2**). They have been fitting thanks to a mixed Gaussian/Lorentzian model with fixed and free parameters.

The bands a and a' (950 cm^{-1} and 961 cm^{-1}) are associated with the $\nu_1\text{PO}_4$ vibration of orthophosphates. The small a' band has this due to the low asymmetry associated with the amorphous band at this main band. The bands b and b' (1036 cm^{-1} and 1044 cm^{-1}) correspond to the main band (iso asymmetrical) of the pyrophosphate ions. Some secondary bands can receive a probable allocation (like c at 1000 cm^{-1} corresponding to HPO_4^{2-}), for) but most of them ((d \rightarrow d') are mainly used to find a linear baseline in the considered domain.

The obtained ratios are area ratios and are related to molecular ratios (taking account of multiplicative constant) that accounts for the difference in absolute intensity of the bands chosen for a standard molecular composition. Moreover, these results do not take into account the alterations of the spectra due to the protonation of the species or to the effects of hydrogen bonds as well. Thus some orthophosphates or protonated pyrophosphates may not be included in their respective categories. Nevertheless, neglecting the relatively low protonation rates and assuming that the absolute intensities of the bands chosen for each species are independent of the composition and local structure of the amorphous species, the results are representative of the variation in the ratios. pyro / ortho.

Table S2. Selection of parameters used for fitting the bands of the Raman spectra.

Name	Entity	Band	Position (cm^{-1})	Parameters of band			
				Max shift (cm^{-1})	Distribution fonction $0 < g < 1$	Width (cm^{-1})	Intensity
a	PO_4^{3-}	$\nu_1\text{PO}_4$	950	+/-10	Non fixed	Non fixed	Non fixed
a'	PO_4^{3-}	$\nu_1\text{PO}_4$	961	+/-10			
b	$\text{P}_2\text{O}_7^{4-}$	$\nu_{\text{as}}\text{PO}_3$	1036	+/-10			
b'	$\text{P}_2\text{O}_7^{4-}$	$\nu_{\text{as}}\text{PO}_3$	1044	+/-10			
c	HPO_4^{2-}	$\nu_s\text{PO}_3$	1000	+/-10			
d	-	-	895	+/-10			
d'	-	-	1080	+/-10			
d''	-	-	1125	+/-10			
d'''	-	-	1176	+/-10			

$0 < g < 1$ with $g = 1$: 100% Gaussian distribution and $g = 0$: 100% Lorentzian

SI-4: ^{31}P CP-INADEQUATE and CPMAS solid state NMR spectra.

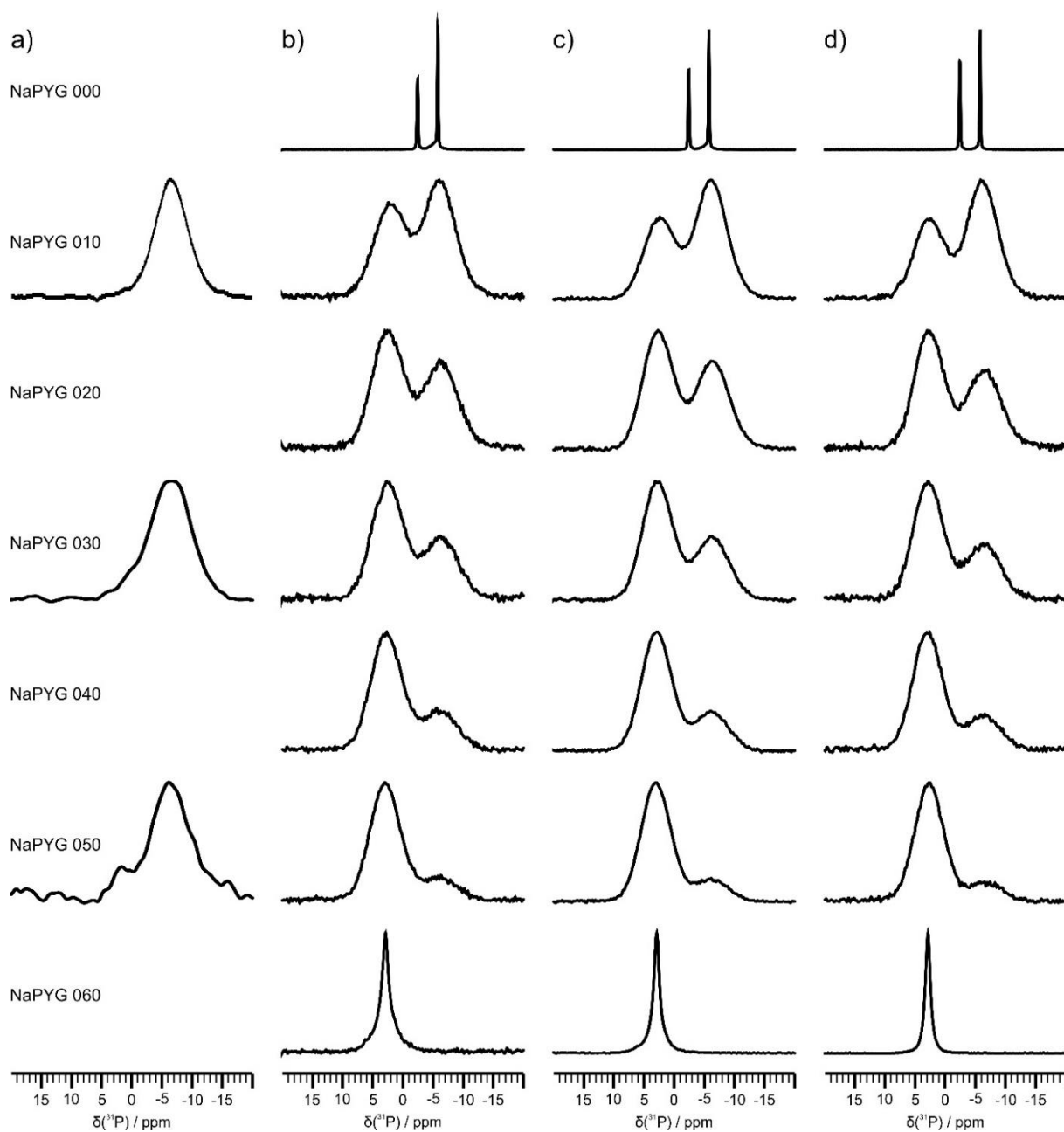


Figure S1. ^{31}P MAS NMR experiments, recorded at 14.1 T, using a) CP-INADEQUATE and b-d) CPMAS sequences (with contact times of b) 300 μs , c) 2 ms, and d) 8 ms). The high frequency shoulder observed on the CP-INADEQUATE spectrum of NaPYG-050 material shows that some pyrophosphate units can resonate at higher frequencies in the orthophosphate region. Additional INADEQUATE experiments were performed to take this into account in the quantifications of Table 2.

SI-5: ^{23}Na solid state NMR data, including spectral deconvolutions.

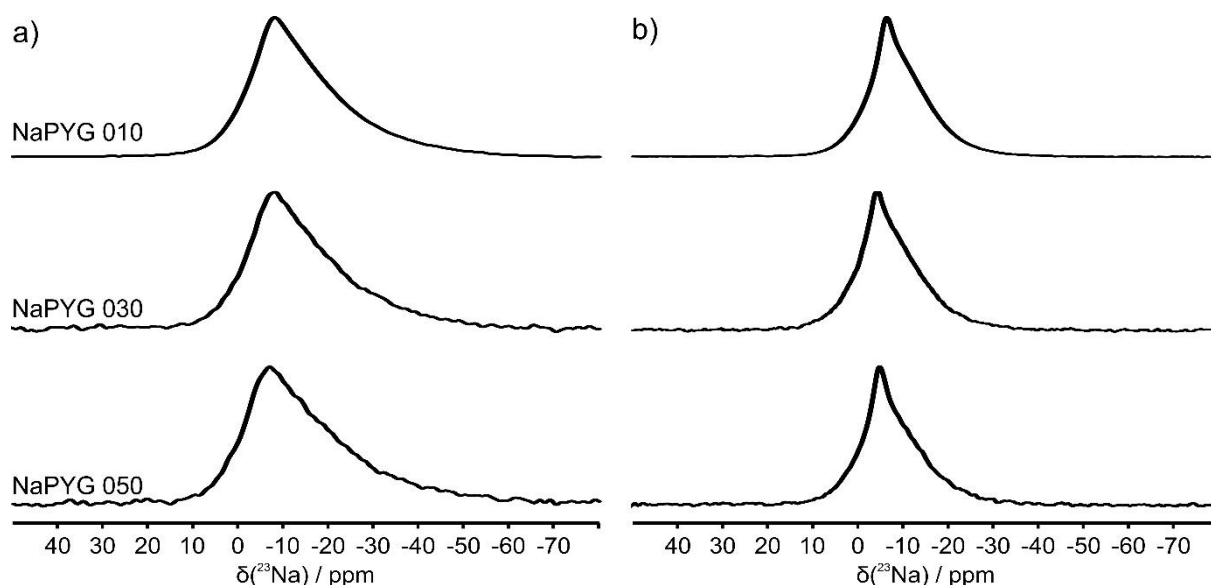


Figure S2. ^{23}Na MAS NMR single pulse spectra recorded using 20 kHz spinning speed, recorded at a) 9.4 T, and b) 14.1 T.

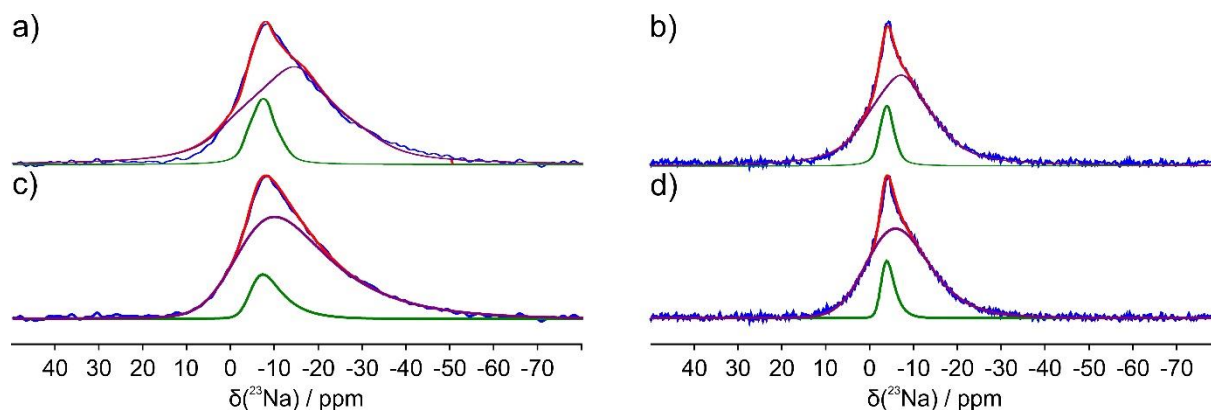


Figure S3.: Deconvolutions (using DMFit⁵) of the ^{23}Na single pulse experiments of NaPYG-030 material, recorded at 9.4 T (left) and 14.1 T (right). Deconvolutions were performed either using a standard quadrupole model (a and b), or a Czjzek model (c and d). A better fit is observed at lower field using a Czjzek model (see a vs c). Results of the relative proportions of the two sites for this sample (and others) are provided in Table S3.

Fitting parameters in the quadrupole model (a & b):

$\delta_{\text{iso}} = -3(2)$ ppm, $C_Q = 1.4(0.1)$ MHz, $\eta = 0.7(0.1)$ (LB ~ 290(10) Hz) (green)

$\delta_{\text{iso}} = 1(3)$ ppm, $C_Q = 2.5(0.3)$ MHz, $\eta = 0.9(0.1)$ (LB ~ 1300(150) Hz) (purple)

Fitting parameters in the Czjzek model (c & d):

$\delta_{\text{iso}} = -1(3)$ ppm, $C_Q = 1.4(0.1)$ MHz (green)

$\delta_{\text{iso}}(^{23}\text{Na}) = 2(3)$ ppm, $C_Q = 2.4(0.2)$ MHz (purple).

⁵ D. Massiot, F. Fayon, M. Capron, I. King, S. Le Calvé, B. Alonso, J.O. Durand, B. Bujoli, Z. Gan, G. Hoatson, Magn. Reson. Chem. 40 (2002) 70–76.

Table S3. Relative proportions of the two ^{23}Na signals in each sample, as determined from fits at two fields (9.4 and 14.1 T), using a standard quadrupolar model or a Czjzek model (see Figure S3 for an example of these deconvolutions). The error on these proportions is estimated to be below 5%.

Sample	Standard quadrupolar model		Czjzek model	
	Narrow site %	Broad site %	Narrow site %	Broad site %
NaPYG-010	21	79	19	81
NaPYG-020	17	83	20	80
NaPYG-030	15	85	17	83
NaPYG-040	20	80	22	78
NaPYG-050	17	83	16	84

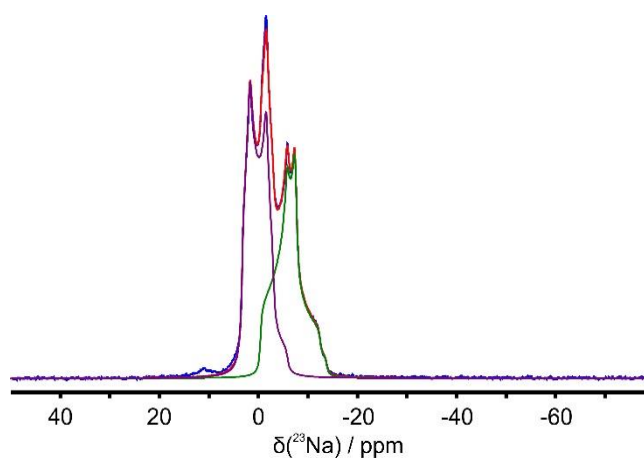


Figure S4. Deconvolution (using DMFit⁶) the ^{23}Na single pulse spectrum of NaPYG-000 material (in blue), recorded at 14.1T (deconvolution using a standard quadrupole model)

- Site 1 (purple): $\delta_{\text{iso}} = 4.0$ (0.1) ppm, $C_Q = 2.00$ (0.05) MHz, $\eta = 0.30$ (0.02)
- Site 2 (green): $\delta_{\text{iso}} = -0.3$ (0.1) ppm, $C_Q = 2.20$ (0.05) MHz, $\eta = 0.78$ (0.02)
- In red: sum of the two sites

⁶ D. Massiot, F. Fayon, M. Capron, I. King, S. Le Calvé, B. Alonso, J.O. Durand, B. Bujoli, Z. Gan, G. Hoatson, *Magn. Reson. Chem.* 40 (2002) 70–76.

SI-6: ^{43}Ca solid state NMR data of NaPYG materials, recorded at both 20.0 T and 35.2T.

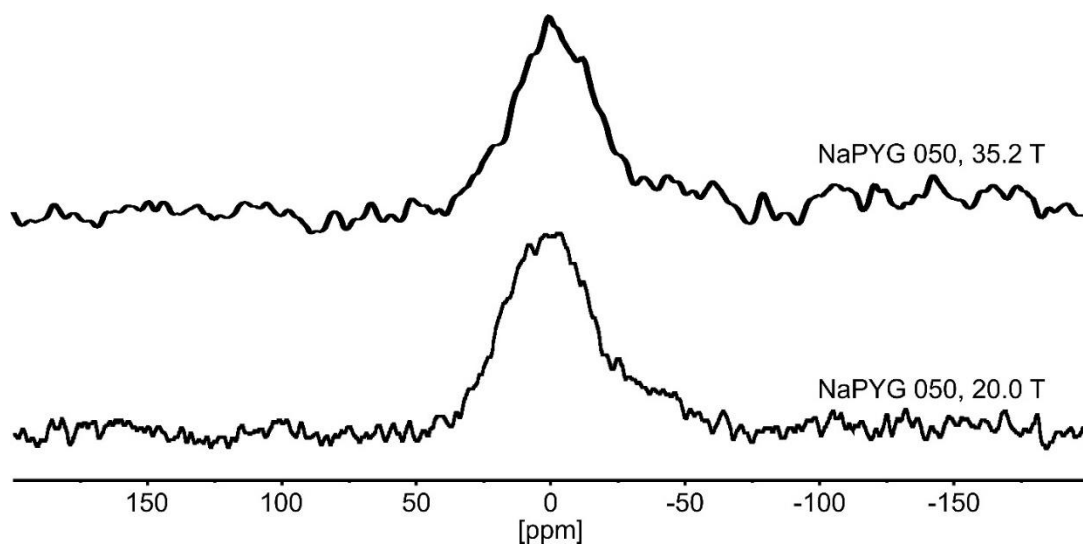


Figure S5. ^{43}Ca MAS NMR of NaPYG-050 material, acquired at 20.0 T and 35.2 T (see SI-2 and Table S1 for all acquisition parameters). The strong similarity between the spectra obtained at the two fields points to the fact the overall ^{43}Ca linewidth is mainly due to chemical shift distribution at these fields.

SI-7: TGA and DTA of NaPYG-020, NaPYG-030, NaPYG-040, NaPYG-050 samples and focus on curves for the other samples

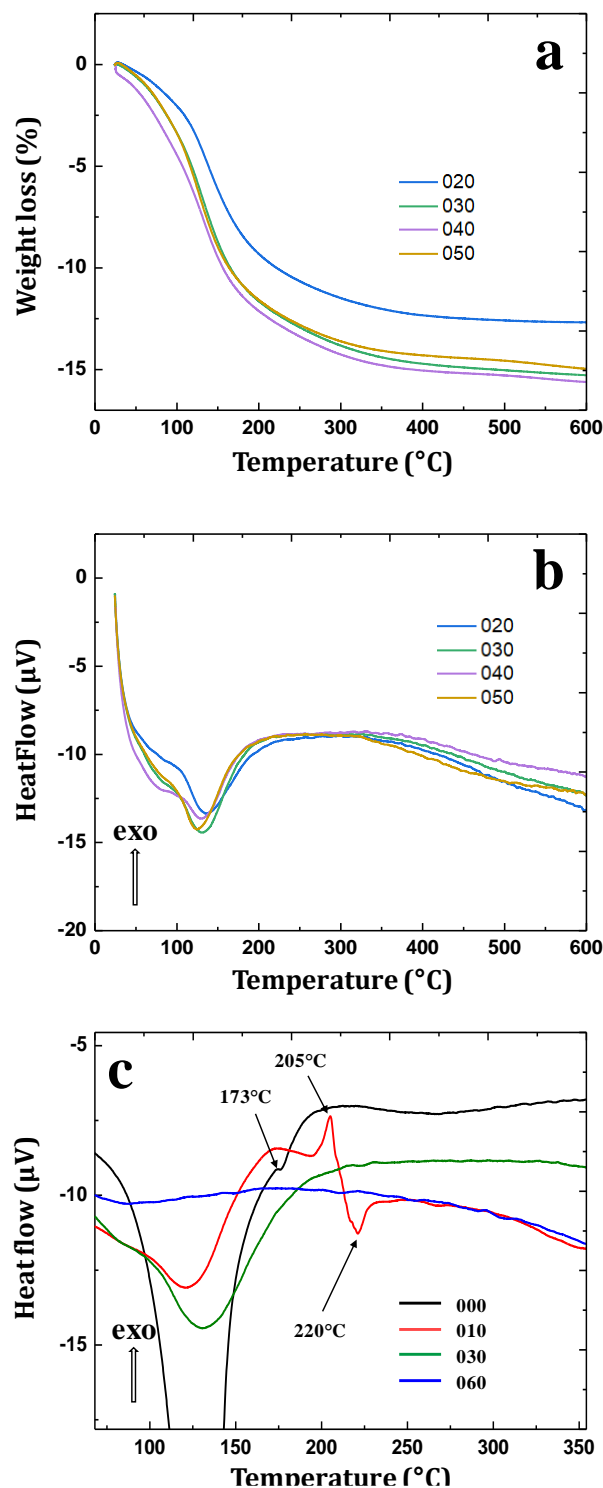


Figure S6. (a) TGA and (b) DTA of NaPYG-020, NaPYG-030, NaPYG-040 and NaPYG-050 materials. The corresponding data for NaPYG-000, NaPYG-010, NaPYG-030, and NaPYG-060 materials is in the core of the text (Figure 4). (c) Focus on the DTA curves between 40 and 360°C for NaPYG000, 010, 030 and 060 materials.

SI-8: Mass percentages of Ca²⁺, Na⁺, PO₄³⁻, P₂O₇⁴⁻ and H₂O in NaPYG materials.

	Ca ²⁺	Na ⁺	PO ₄ ³⁻	P ₂ O ₇ ⁴⁻	H ₂ O	Σ masses (g)
NaPYG000	12.82 ± 0.10	13.40 ± 0.07	0 ± 0	51.4 ± 1.2	20.13 ± 0.50	97.76 ± 2.00
NaPYG010	24.85 ± 0.10	2.30 ± 0.07	14.8 ± 0.3	38.6 ± 0.9	13.66 ± 0.50	94.15 ± 2.00
NaPYG020	25.85 ± 0.20	2.30 ± 0.07	23.2 ± 0.5	29.3 ± 0.7	12.67 ± 0.50	93.30 ± 2.00
NaPYG030	26.81 ± 0.10	1.38 ± 0.07	27.0 ± 0.8	24.7 ± 0.8	15.29 ± 0.50	95.15 ± 2.00
NaPYG040	27.49 ± 0.10	0.69 ± 0.07	32.6 ± 0.4	17.5 ± 0.2	15.62 ± 0.50	93.95 ± 1.00
NaPYG050	26.93 ± 0.20	0.69 ± 0.07	36.5 ± 0.5	11.8 ± 0.2	14.98 ± 0.50	90.90 ± 1.00
NaPYG060	30.94 ± 0.20	0.46 ± 0.07	51.3 ± 0.5	0 ± 0	4.95 ± 0.50	87.64 ± 1.00

Table S4. Mass percentages of Ca²⁺, Na⁺, PO₄³⁻, P₂O₇⁴⁻ and H₂O for 100 g of NaPYG material, as determined by ICP-OES, ³¹P solid state NMR and TGA analysis results.

SI-9: TEM picture of NaPYG030 material

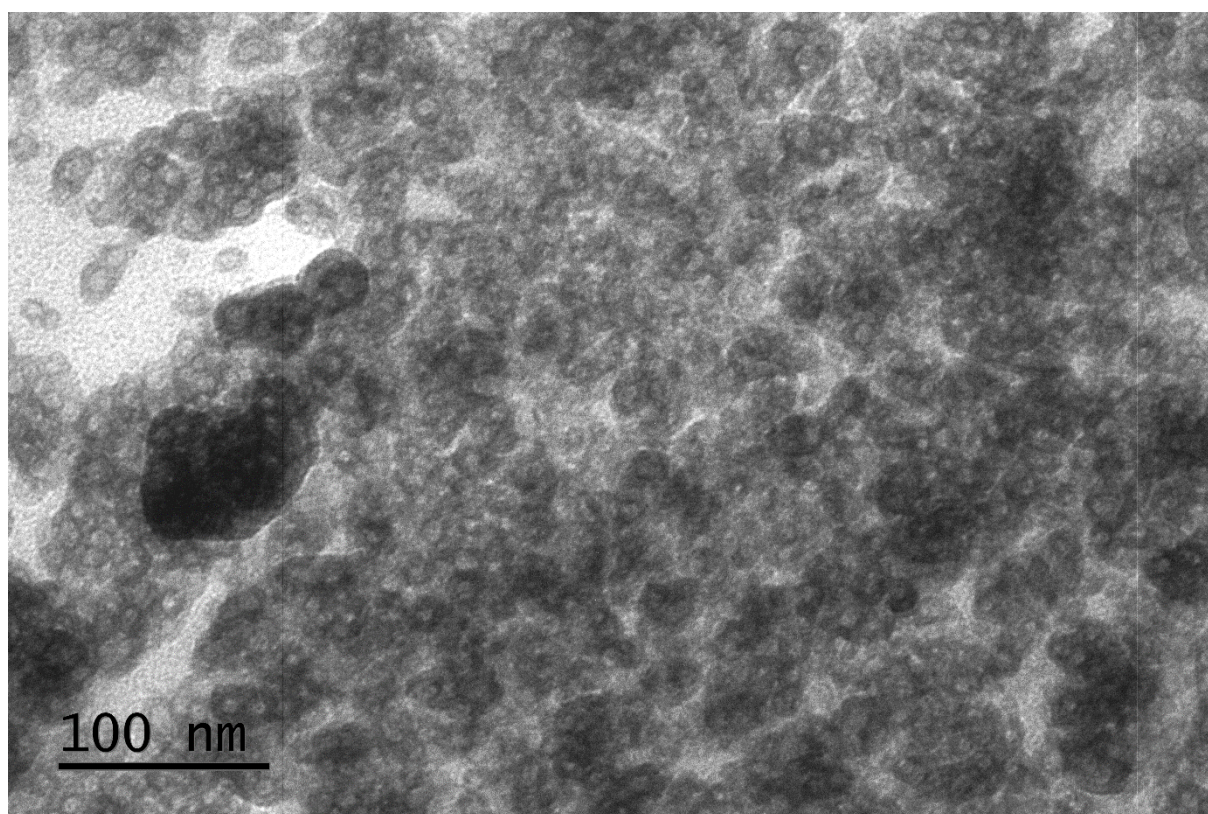


Figure S7. TEM picture of NaPYG-030 ; JEM-1400 electron microscope/JEOL measurement (W filament, voltage of 120 kV), carried out on thin cut of samples embedded in resin.

SI-10: Comparison of ^{23}Na and ^{31}P NMR spectra of NaPYG-010 materials from different synthetic batches.

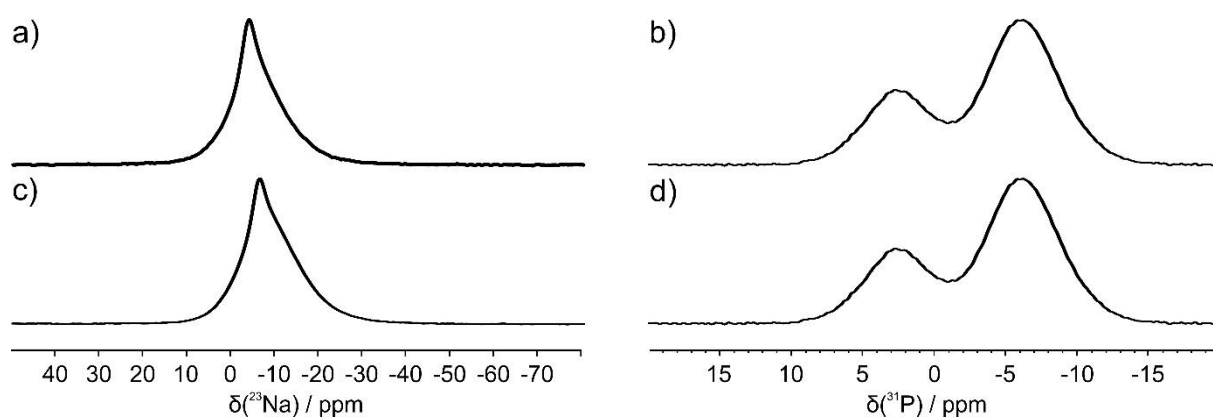


Figure S8. Comparison of ^{23}Na (left) and ^{31}P (right) MAS NMR spectra recorded at 14.1 T, for NaPYG-010 material from different synthetic batches. The strong similarity between the spectra points to the reproducibility of the syntheses.

SI-11: ^1H Hahn echo spectra of NaPYG phases, and $^1\text{H} \rightarrow ^{31}\text{P}$ HETCOR study of NaPYG-010 material.

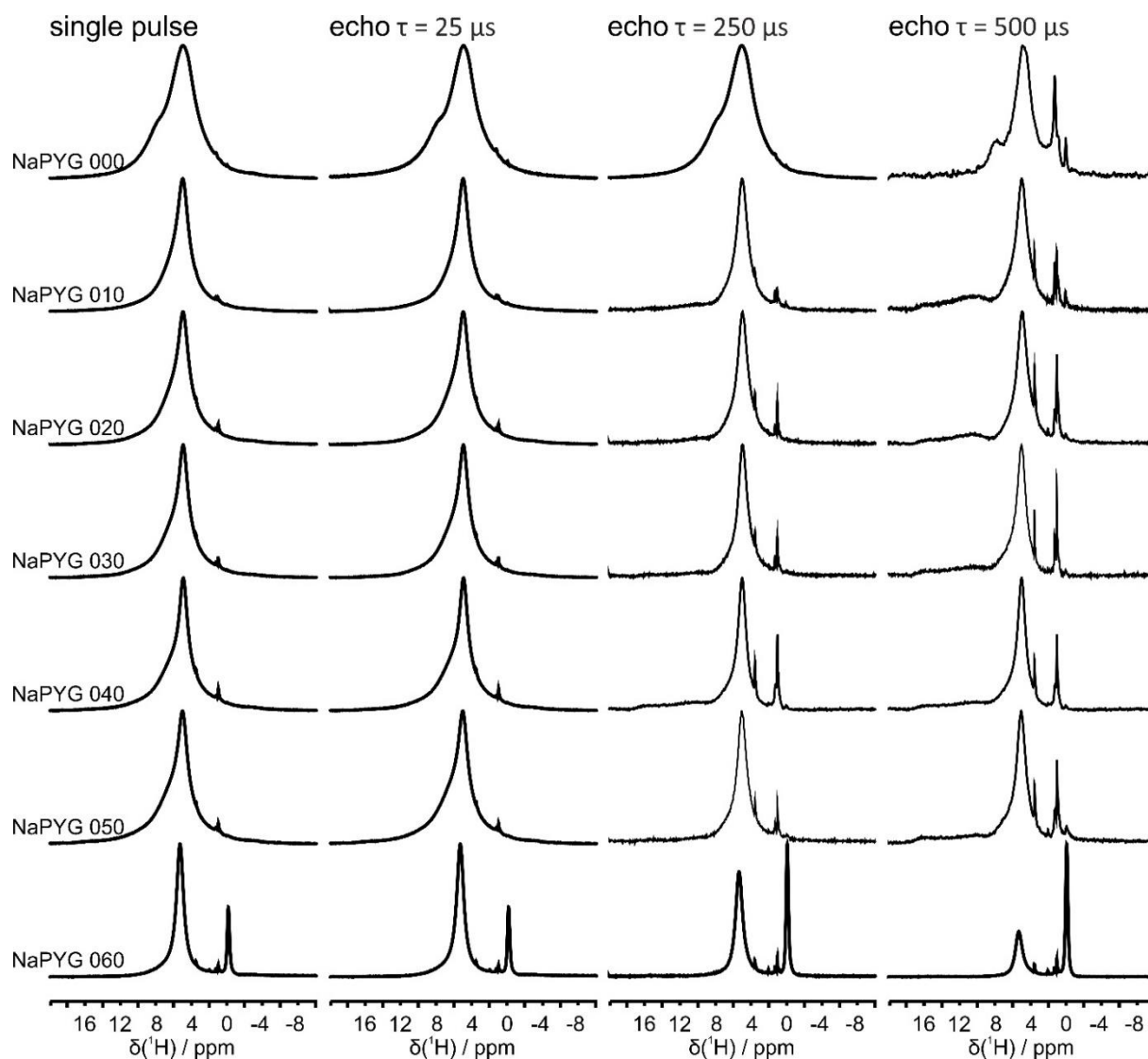


Figure S9. ^1H single pulse and Hahn echo MAS NMR spectra, acquired at 14.1 T, using 40 kHz spinning speed, with echo delays of $\tau = 25 \mu\text{s}$, $250 \mu\text{s}$ and $500 \mu\text{s}$. The sharp resonances observed for the longer echo delays for compounds NaPYG-000 to NaPYG-050 materials correspond to more mobile ^1H environments, which may come from residual solvent contributions. For NaPYG-060 material, the sharp signal centered at 0 ppm is assigned to the hydroxyl groups of nanocrystalline apatite.

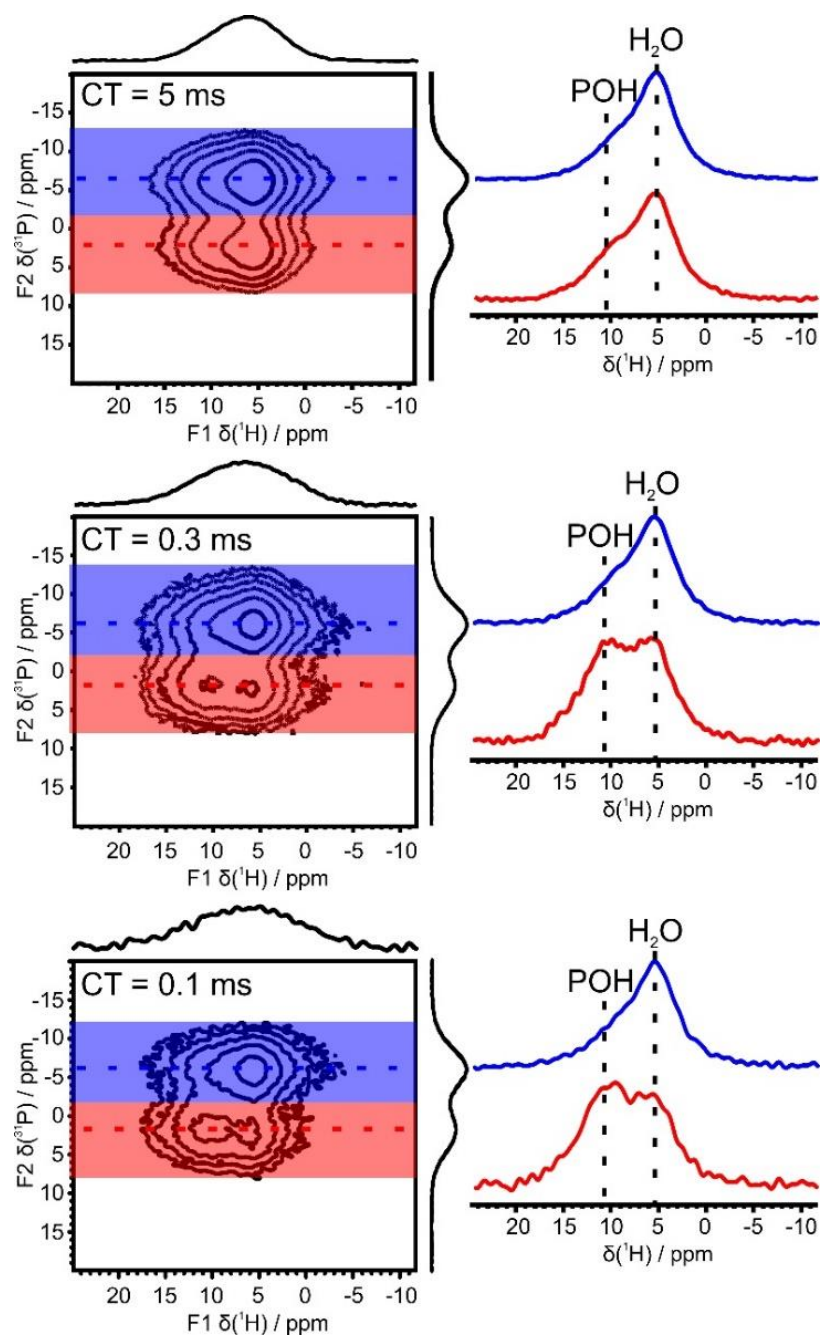


Figure S10. $^1\text{H} \rightarrow ^{31}\text{P}$ HETCOR spectra of NaPYG-010 material, acquired at 14.1 T spinning at 22 kHz, and using different contact times (0.1, 0.3 and 5.0 ms). The ^1H projections on the 2D spectra correspond to the summed intensity. The ^1H 1D spectra on the right are the slices corresponding to correlations with ^{31}P resonances of ortho- and pyrophosphate units, in red and blue, respectively.

SI-12: XRD diagrams and Raman spectra of NaPYG materials obtained without the washing step.

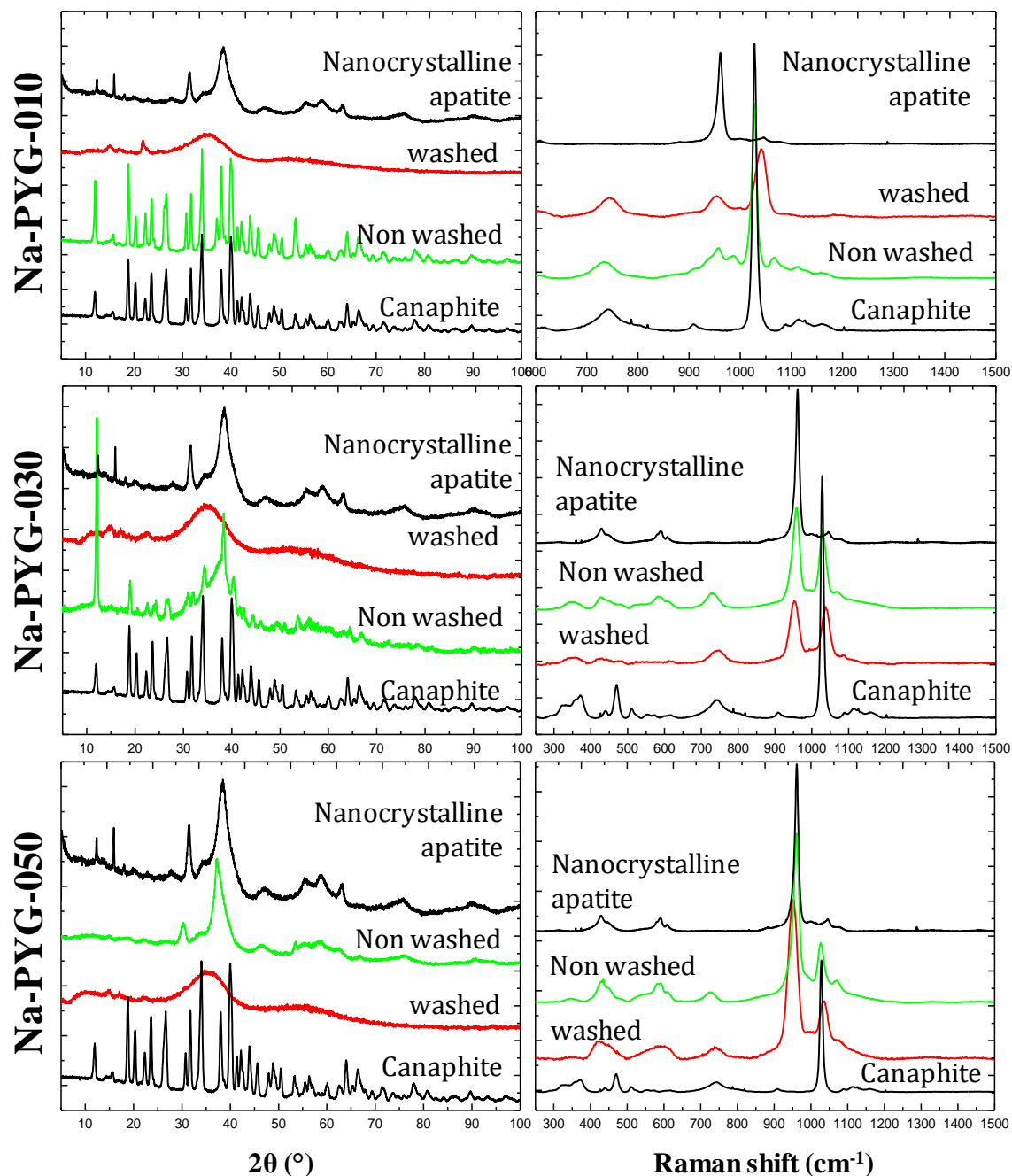


Figure S12. XRD diagrams (left) and Raman spectra (right) of NaPYG materials obtained without the washing step (green), in comparison to the washed materials (red) and to the crystalline reference materials (black). XRD Measurements have been achieved with a with a Cobalt anticathode ($\lambda(K_{\alpha\text{average}}) = 1.7903 \text{ \AA}$).